

# An Added-Mass Partition Algorithm for Fluid-Structure Interactions of Compressible Fluids and Nonlinear Solids

J. W. Banks<sup>a,1,2</sup>, W. D. Henshaw<sup>a,1,3,\*</sup>, A. K. Kapila<sup>a,4</sup>, D. W. Schwendeman<sup>a,1,3,4</sup>

<sup>a</sup>*Department of Mathematical Sciences, Rensselaer Polytechnic Institute, Troy, NY 12180, USA*

---

## Abstract

We describe an added-mass partitioned (AMP) algorithm for solving fluid-structure interaction (FSI) problems involving inviscid compressible fluids interacting with nonlinear solids that undergo large rotations and displacements. The computational approach is a mixed Eulerian-Lagrangian scheme that makes use of deforming composite grids (DCG) to treat large changes in the geometry in an accurate, flexible, and robust manner. The current work extends the AMP algorithm developed in Banks et al. [1] for linearly elastic to the case of nonlinear solids. To ensure stability for the case of *light* solids, the new AMP algorithm embeds an approximate solution of a nonlinear fluid-solid Riemann (FSR) problem into the interface treatment. The solution to the FSR problem is derived and shown to be of a similar form to that derived for linear solids: the state on the interface being fundamentally an impedance-weighted average of the fluid and solid states. Numerical simulations demonstrate that the AMP algorithm is stable even for light solids when added-mass effects are large. The accuracy and stability of the AMP scheme is verified by comparison to an exact solution using the method of analytical solutions and to a semi-analytical solution that is obtained for a rotating solid disk immersed in a fluid. The scheme is applied to the simulation of a planar shock impacting a light elliptical-shaped solid, and comparisons are made between solutions of the FSI problem for a neo-Hookean solid, a linearly elastic solid, and a rigid solid. The ability of the approach to handle large deformations is demonstrated for a problem of a high-speed flow past a light, thin, and flexible solid beam.

*Keywords:* Fluid-structure interaction, compressible fluid flow, hyperelastic solids, Riemann problems, added-mass partitioned methods, moving overlapping grids.

---

---

\*Department of Mathematical Sciences, Rensselaer Polytechnic Institute, 110 8th Street, Troy, NY 12180, USA.

*Email addresses:* [banksj3@rpi.edu](mailto:banksj3@rpi.edu) (J. W. Banks), [henshw@rpi.edu](mailto:henshw@rpi.edu) (W. D. Henshaw), [kapila@rpi.edu](mailto:kapila@rpi.edu) (A. K. Kapila), [schwed@rpi.edu](mailto:schwed@rpi.edu) (D. W. Schwendeman)

<sup>1</sup>This work was supported by contracts from the U.S. Department of Energy ASCR Applied Math Program.

<sup>2</sup>Research supported by a U.S. Presidential Early Career Award for Scientists and Engineers.

<sup>3</sup>Research supported by the National Science Foundation under grant DMS-1519934.

<sup>4</sup>Research supported by the National Science Foundation under grants DMS-1016188.

## Contents

<b>1</b>	<b>Introduction</b>	<b>3</b>
<b>2</b>	<b>Governing equations</b>	<b>5</b>
<b>3</b>	<b>Fluid-solid Riemann problem and the AMP interface projection</b>	<b>7</b>
3.1	Rotated equations . . . . .	8
3.2	AMP interface projections . . . . .	9
<b>4</b>	<b>The FSI-DCG numerical approach for initial-boundary-value problems</b>	<b>11</b>
4.1	Deforming composite grids . . . . .	11
4.2	Discretization of the fluid and solid governing equations . . . . .	12
4.3	FSI-DCG time-stepping algorithm with AMP projection . . . . .	17
<b>5</b>	<b>Convergence tests</b>	<b>18</b>
5.1	The method of analytic solutions . . . . .	18
5.2	Rotating disk . . . . .	20
<b>6</b>	<b>Interaction of a planar shock and an elliptical solid</b>	<b>24</b>
<b>7</b>	<b>Flexible solid beam in a cross flow</b>	<b>30</b>
<b>8</b>	<b>Conclusions</b>	<b>32</b>

## 1. Introduction

Fluid-structure interaction (FSI) problems are important in many fields of engineering and applied science. These problems are often difficult to simulate in an efficient, stable and accurate manner. One important issue that arises in many FSI simulations is the treatment of large changes in geometry such as those arising when solid bodies or structures undergo large rotations and deformations. To address this challenge we use a mixed Eulerian-Lagrangian approach together with deforming composite grids (DCG) that can flexibly and efficiently treat these large changes in geometry while retaining high quality grids [1]. A second important issue concerns the stability of the overall FSI algorithm and the numerical treatment of the interface between the fluid and solid domains. This is especially important for the case of partitioned solvers<sup>5</sup>. To address this issue we have developed a variety of *added-mass partitioned* (AMP) algorithms that embed analytically derived interface conditions into the numerical approximation at the interface as a means to obtain accurate and stable partitioned algorithms, even for *light* solids when added-mass effects are large. The form of the derived interface conditions depends on the regime of the FSI problem. For the case of inviscid compressible fluids coupled to rigid solids [2], for example, the derived AMP interface conditions incorporate added-mass tensors into the rigid-body equations that stabilize the AMP scheme when the mass of the body is small, or even zero. For cases involving deformable solids, on the other hand, the derived AMP interface conditions take the form of mixed (Robin) type conditions involving the velocity and stress; the coefficients in the mixed interface conditions account for the added mass effects. This approach was first used in [1, 3] for the case of inviscid compressible fluids coupled to a linearly elastic solids, and later extended to FSI regimes involving *incompressible* fluids coupled to either compressible elastic bulk solids [4] or elastic structural shells [5, 6]. A principal aim of the present paper is to extend the analysis in [1] and develop an AMP algorithm for inviscid compressible fluids coupled to nonlinear hyperelastic solids. This new AMP algorithm is applicable to a large class of FSI problems, such as those involving large solid deformations and rotations.

We consider a mixed Eulerian-Lagrangian formulation of the FSI problem. The equations governing the fluid are formulated in *physical (Eulerian) space* with evolving boundaries, and are given by the equations of gas dynamics with an ideal equation of state. For the solid, we formulate the governing equations in a static *reference (Lagrangian) space*, and write these equations as a first-order system for the components of displacement, velocity and nominal stress. A constitutive law relating the stress tensor to the deformation gradient tensor completes the system of equations for the solid. We consider the class of hyperelastic solids which implies a nonlinear constitutive law in general. The mathematical formulation of the FSI problem is closed by specifying initial conditions, by imposing matching conditions for velocity and stress on the deforming fluid-solid interface, and by assigning suitable boundary conditions on the remaining portions of the fluid and solid domains.

The equations governing the fluid and solid are both systems of nonlinear hyperbolic partial differential equations (assuming certain conditions on the deformation in the solid depending on the choice of constitutive law). The equations are solved numerically on DCGs. For the fluid, we use a general arbitrary Lagrangian-Eulerian (ALE) formulation of the equations on moving grids, and solve the equations using a second-order extension of Godunov’s method with an approximate Roe Riemann solver. This Godunov scheme is described in [7] for static boundaries, and extended in [8] for moving boundaries. The numerical treatment of the equations in the fluid domain are well described elsewhere and we provide only a very brief description in this paper for completeness. For the solid, the equations are mapped to a static computational space and solved on overlapping grids using a new second-order accurate, characteristics-based upwind method, which extends the approach in [9] to nonlinear elasticity. The characteristics of the system of equations for the solid with nonzero wave speed correspond to pressure and shear waves. There are also characteristics with zero wave speed corresponding to the tangential components of stress and the components of displacement. The upwind scheme for the solid adds no dissipation to the characteristic variables associated with these zero wave speeds, and this can lead to numerical instabilities for certain problems. To suppress these instabilities, we add small high-order dissipation terms to the components of the solution corresponding to the zero wave speeds.

---

<sup>5</sup>Partitioned algorithms, unlike monolithic algorithms, make use of separate solvers for the fluid and solid domains.

There are two other (related) issues that arise when solving the first-order system for the evolution of the solid. The first issue concerns the compatibility between the stress and strain. For the first-order system, we evolve the time derivative of the stress-strain relation,  $\bar{P} = \bar{\mathcal{P}}(\bar{F})$ , where  $\bar{P}$  and  $\bar{F}$  denote the nominal stress and deformation gradient tensors, respectively, and thus the numerical solution can drift from satisfying the stress-strain relation. This drift can be suppressed by adding a stress-strain relaxation term (penalty term) to the evolution equation for  $\bar{P}$  following the approach used in [1]. The second issue is that although the momentum equation is in conservation form, the evolution equation for  $\bar{P}$  is not. This is a potential issue when solving problems with discontinuous jumps in the velocity that can occur, for example, when a fluid shock impacts the solid. In this case we have found that use of the stress-strain relaxation term can ameliorate issues related to the non-conservative form. This derives from the fact that satisfaction of the stress-strain relation together with the conservative treatment of the momentum equation would lead to the correct weak solution for convergent numerical schemes. We note that there are alternative conservative formulations of the first-order system, such as the one considered by Miller and Colella [10], for example.

The coupling of the numerical solutions for the fluid and solid is performed at the fluid-solid interface using an *interface projection scheme*. The scheme embeds an approximate solution of a nonlinear fluid-solid Riemann (FSR) problem into the numerical treatment of the interface. The solution to the FSR problem leads to formulas for the projected states of velocity and stress that are impedance-weighted averages of the predicted fluid and solid states adjacent to the interface. These formulas, which we refer to as the *full projection*, are extensions of the ones derived in [1] for a linearly-elastic solid. In addition to the full projection, we also derive a *simplified projection* which is easier to implement and computationally less costly. Numerical results indicate that the simplified projection provides nearly identical results to those given by the full projection for the problems considered. The new AMP scheme based on the full or simplified projection remains stable even for light solids when added-mass effects are large.

The AMP algorithm based on the interface projection scheme, either full or simplified, is fundamentally different than the traditional partitioned approach to FSI problems, even though both approaches can make use of solutions of Riemann problems in their implementation. Farhat et al. [11, 12], for example, employ a *one-sided* Riemann problem at the fluid-solid interface, in which the state of the fluid at the interface is determined for a *given* solid displacement and velocity of the interface. Thus, this interface treatment has the form of a traditional partitioned approach in which the solid velocity and displacement determine the motion of the fluid at the interface, while the fluid stress is applied as a traction condition on the solid. In contrast, the present AMP algorithm uses an interface projection scheme based on a *two-sided* fluid-solid Riemann problem leading to impedance-weighted averages for the interface velocity and stress for the fluid and solid. An interesting consequence of this AMP approach is that for very light solids, the position and velocity of the interface are determined by the *fluid* and not by the solid as in the traditional approach.

A number of FSI model problems of varying complexity are considered to demonstrate the use of the new AMP scheme and to evaluate its accuracy and stability. The method of analytic solutions is used to construct an exact solution of an FSI problem for an elastic-piston geometry. Maximum-norm errors in the components of the solution are computed for this problem for composite grids of varying resolution to verify second-order accuracy of the AMP scheme. A more complex FSI problem involving a rotating solid disk in a surrounding fluid is considered to verify the accuracy and stability of the AMP scheme for light, medium and heavy solids. A semi-analytic exact solution is derived for this problem and used to determine the maximum-norm errors in the solution of the AMP algorithm. Second-order accuracy is verified for this problem, and stability is demonstrated even for the difficult case of a light solid when added-mass effects are large. We also consider an FSI problem involving the impact of a planar shock and a light elliptical-shaped solid. The problem is computed for two different hyperelastic solid models, namely, neo-Hookean and linear elasticity, and for a third case which assumes that the solid is rigid. In the latter case, the FSI problem is solved using the AMP scheme described in [2] for light rigid solids. The aim of this last test problem is to show that the AMP scheme is accurate and stable for a range of solid models, and to demonstrate the FSI-DCG approach for a problem with significant and complex solid rotation and deformation. Finally the capability of the scheme to handle very large deformations is illustrated through the simulation of flow past a light and flexible solid beam.

A wide variety of numerical techniques have been and continue to be developed for solving FSI problems; this is a reflection of the importance and broad scope of this active field of research. Some of these numerical approaches include those based on Eulerian, Lagrangian, Arbitrary Lagrangian-Eulerian (ALE)

methods [13–16], immersed boundary methods [17, 18], embedded boundary methods [19], level-set methods [20, 21], interface tracking schemes [22, 23], and distributed-Lagrange-multiplier/fictitious-domain methods [24]. Numerical approximations based on finite-element [25], finite-volume [10, 26] and discontinuous Galerkin methods [27], among others, have been developed. Overlapping grids, on the other hand, have been used to solve a wide variety of problems, primarily in the fields of aerodynamics and fluid dynamics, but more recently they have also been applied to electromagnetics [28] and solid mechanics [9]. Overlapping grids were recognized early on to be a useful technique for treating rigid moving bodies, such as aircraft store separation [29], and have subsequently been applied to many other moving-grid aerodynamic applications, see for example [8, 30–33].

The remaining sections of the paper are arranged as follows. The governing equations for the fluid and solid are given in Section 2; this includes a discussion of the solid constitutive models and the interface conditions. The solution of the fluid-solid Riemann problem is given in Section 3 and the full and simplified AMP interface projections are derived. The FSI time-stepping algorithm that incorporates the AMP projection is outlined in Section 4. This section also includes a discussion of the DCG approach as well as short descriptions of the numerical approaches used to solve the fluid and solid equations in their respective domains. Numerical results for FSI problems involving an elastic piston and a rotating disk are described in Section 5, while results for the shock-solid impact problem are discussed in Section 6. Results for a solid beam in a cross flow are presented in Section 7, and concluding remarks are given in Section 8.

## 2. Governing equations

We consider the interaction of an inviscid, compressible fluid coupled to a compressible elastic solid. Let us assume that the fluid occupies the domain  $\mathbf{x} \in \Omega(t)$  for time  $t \geq 0$ . The equations governing the evolution of the fluid can be written (with Einstein summation convention) in conservation form as

$$\frac{\partial}{\partial t} q_i + \frac{\partial}{\partial x_j} f_{ij}(\mathbf{q}) = 0, \quad \mathbf{x} \in \Omega(t), \quad t \geq 0, \quad (1)$$

where  $\mathbf{q}$ , with components  $q_i$ , is a vector of conserved fluid variables and  $\mathbf{f}$ , with components  $f_{ij}$ , contains the corresponding fluxes. Here the integer indices  $i$  and  $j$  range from 1 to  $n_d$ , the number of space dimensions. We consider the inviscid Euler equations with  $\mathbf{q} = [\rho, \rho\mathbf{v}, \rho\mathcal{E}]^T$  and  $\mathbf{f} = [\rho\mathbf{v}, \rho\mathbf{v} \otimes \mathbf{v} + pI, (\rho\mathcal{E} + p)\mathbf{v}]^T$ , where  $\rho$  is the density,  $\mathbf{v}$  is the velocity with components  $v_i$ , and  $p$  is the pressure. The total energy is given by  $\rho\mathcal{E} = p/(\gamma - 1) + \frac{1}{2}\rho|\mathbf{v}|^2$  assuming an ideal gas with a constant ratio of specific heats,  $\gamma$ .

The governing equations for the elastic solid are written in terms of the reference coordinates  $\bar{\mathbf{x}}$ , with components  $\bar{x}_i$ , and it is assumed that the solid occupies the domain  $\bar{\mathbf{x}} \in \bar{\Omega}_0$  at  $t = 0$ . In the reference space, the equations for the solid are

$$\bar{\rho} \frac{\partial^2 \bar{u}_i}{\partial t^2} = \frac{\partial \bar{P}_{ji}}{\partial \bar{x}_j}, \quad \bar{\mathbf{x}} \in \bar{\Omega}_0, \quad t \geq 0, \quad (2)$$

where  $\bar{\rho}$  is the density of the solid in its reference configuration, assumed to be spatially uniform,  $\bar{\mathbf{u}}$ , with components  $\bar{u}_i$ , is the displacement of the solid, and  $\bar{P}_{ij}$  are components of the nominal stress tensor. The physical domain of the solid,  $\mathbf{x} \in \bar{\Omega}(t)$  for  $t \geq 0$ , corresponding to the reference domain,  $\bar{\mathbf{x}} \in \bar{\Omega}_0$ , is determined from the computed displacement as

$$\mathbf{x} = \phi(\bar{\mathbf{x}}, t) = \bar{\mathbf{x}} + \bar{\mathbf{u}}(\bar{\mathbf{x}}, t), \quad \bar{\mathbf{x}} \in \bar{\Omega}_0, \quad t \geq 0.$$

An assumed constitutive law,  $\bar{P} = \bar{P}(\bar{F})$ , discussed below, relates  $\bar{P}$  to the deformation gradient tensor,  $\bar{F}$ , which is given in terms of the displacement by

$$\bar{F} \equiv \frac{\partial \mathbf{x}}{\partial \bar{\mathbf{x}}} = I + \frac{\partial \bar{\mathbf{u}}}{\partial \bar{\mathbf{x}}}. \quad (3)$$

For purposes of discretization, we consider the equations in (2) as a first-order system

$$\left. \begin{aligned} \frac{\partial \bar{u}_i}{\partial t} &= \bar{v}_i \\ \bar{\rho} \frac{\partial \bar{v}_i}{\partial t} &= \frac{\partial \bar{P}_{ji}}{\partial \bar{x}_j} \\ \frac{\partial \bar{P}_{ij}}{\partial t} &= \bar{K}_{ijkl} \frac{\partial \bar{v}_k}{\partial \bar{x}_l} \end{aligned} \right\}, \quad \bar{\mathbf{x}} \in \bar{\Omega}_0, \quad t \geq 0, \quad (4)$$

where  $\bar{v}_i$  are the components of the solid velocity and the stress-strain tensor  $\bar{K}_{ijkl} = \bar{K}_{ijkl}(\bar{F})$  is defined from the constitutive law by

$$\bar{K}_{ijkl} = \frac{\partial \bar{P}_{ij}}{\partial \bar{F}_{kl}}. \quad (5)$$

The first-order system of equations in (4) can also be written in the quasilinear matrix form

$$\frac{\partial \bar{q}_i}{\partial t} + \bar{A}_{ijk}(\bar{\mathbf{q}}) \frac{\partial \bar{q}_j}{\partial \bar{x}_k} = \bar{b}_i(\bar{\mathbf{q}}), \quad \bar{\mathbf{x}} \in \bar{\Omega}_0, \quad t \geq 0, \quad (6)$$

where  $\bar{\mathbf{q}}$ , with components  $\bar{q}_i$ , is the vector of solid variables that includes the components of  $\bar{\mathbf{u}}$ ,  $\bar{\mathbf{v}}$ , and  $\bar{P}$ . Finally, we note that the physical Cauchy stress,  $\bar{\boldsymbol{\sigma}}$ , may be computed from the nominal stress and the deformation gradient tensor by

$$\bar{\boldsymbol{\sigma}} = \frac{1}{\bar{J}} \bar{F} \bar{P}, \quad \text{where } \bar{J} = \det(\bar{F}).$$

For the solid constitutive law, we consider hyperelastic materials for which the elastic strain energy  $\bar{\Psi}$  is a given function of the Green strain tensor  $\bar{E}$ ,

$$\bar{\Psi} = \bar{\Psi}(\bar{E}), \quad \bar{E} = \frac{1}{2}(\bar{F}^T \bar{F} - I).$$

For such materials, the nominal stress  $\bar{P}$  is determined by

$$\bar{P} = \bar{S} \bar{F}^T, \quad \bar{S}_{ij} = \frac{\partial \bar{\Psi}}{\partial \bar{E}_{ij}}, \quad (7)$$

where  $\bar{S}$  is the second Piola-Kirchoff (PK2) stress. It follows from (7) that  $\bar{P}_{ij} = \partial \bar{\Psi} / \partial \bar{F}_{ji}$ , and thus

$$\bar{K}_{ijkl} = \frac{\partial^2 \bar{\Psi}}{\partial \bar{F}_{ji} \partial \bar{F}_{kl}}. \quad (8)$$

From (8) we note the major symmetry,  $\bar{K}_{ijkl} = \bar{K}_{ljk i}$ , and this plays an important role in the characteristic form of the system of equations in (6) for the solid as discussed in Section 3.

In this paper, we consider two specific nonlinear constitutive stress-stain laws implied by two choices of the strain energy function  $\bar{\Psi}$ . The first is the Saint Venant-Kirchhoff (SVK) model given by

$$\bar{P} = \bar{S} \bar{F}^T, \quad \bar{S} = \bar{\lambda}(\text{tr } \bar{E}) I + 2\bar{\mu} \bar{E}, \quad (9)$$

where  $\bar{\lambda}$  and  $\bar{\mu}$  are Lamé constants. This constitutive law is implied by the choice

$$\bar{\Psi} = \frac{\lambda}{2} [\text{tr}(\bar{E})]^2 + \mu \text{tr}(\bar{E}^2).$$

The second constitutive law is the neo-Hookean model given by

$$\bar{P} = \bar{S} \bar{F}^T, \quad \bar{S} = \bar{\lambda} \ln(\bar{J}) \bar{C}^{-1} + \bar{\mu} (I - \bar{C}^{-1}), \quad \bar{C} = \bar{F}^T \bar{F}, \quad (10)$$

which is implied by the choice

$$\bar{\Psi} = \frac{1}{2} \lambda [\ln(\bar{J})]^2 - \mu \ln(\bar{J}) + \frac{1}{2} \mu [\text{tr}(\bar{C}) - 3].$$

Both of these constitutive laws reduce to the usual linearly elastic model in the limit of a small displacement gradient, i.e.  $\|\bar{\mathbf{u}}_{\bar{\mathbf{x}}}\| = \|\bar{\mathbf{F}} - I\| \ll 1$ . A third constitutive law, corresponding to linear elasticity, may be written in the form

$$\bar{\mathbf{P}} = \bar{\lambda}(\text{tr } \tilde{\mathbf{E}})I + 2\bar{\mu}\tilde{\mathbf{E}}, \quad \tilde{\mathbf{E}} = \frac{1}{2}(\bar{\mathbf{u}}_{\bar{\mathbf{x}}} + \bar{\mathbf{u}}_{\bar{\mathbf{x}}}^T) = \frac{1}{2}(\bar{\mathbf{F}} + \bar{\mathbf{F}}^T) - I, \quad (11)$$

where  $\tilde{\mathbf{E}}$  is a linear approximation of the Green strain tensor. This latter model was used in [1] and is used here as a reference to compare the linear behavior with results obtained from either of the first two nonlinear hyperelastic constitutive models.

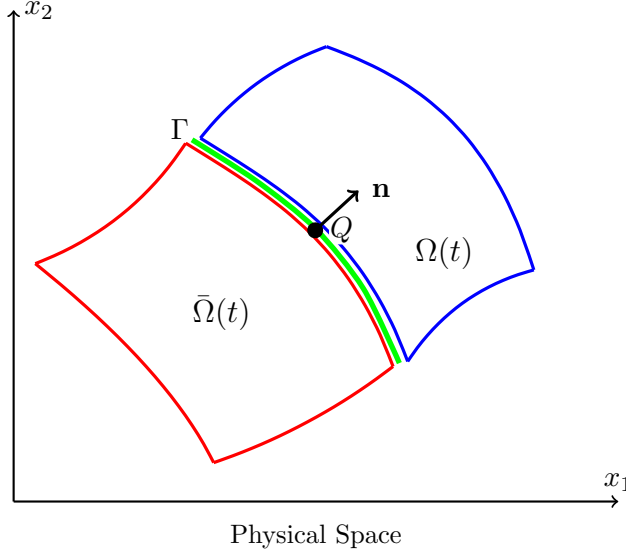


Figure 1: The blue fluid domain  $\Omega(t)$  matches the red solid domain  $\bar{\Omega}(t)$  in physical space along a green interface  $\Gamma$ .  $Q$  is a point on the interface, and  $\mathbf{n}$  the normal to the interface.

It is assumed that the physical domains of the fluid  $\Omega(t)$  and solid  $\bar{\Omega}(t)$  share a common boundary  $\mathbf{x} \in \Gamma(t)$  with unit normal  $\mathbf{n}(t)$  pointing from the solid towards the fluid, see Figure 1. The corresponding boundary of the solid reference domain is denoted by  $\bar{\Gamma}_0$  with unit normal  $\bar{\mathbf{n}}_0$ . For  $\mathbf{x} \in \Gamma(t)$ , the normal components of velocity in the fluid and solid and the stresses must match. These interface conditions are

$$\mathbf{n}^T \mathbf{v} = \mathbf{n}^T \bar{\mathbf{v}}, \quad \mathbf{n}^T \boldsymbol{\sigma} = \mathbf{n}^T \bar{\boldsymbol{\sigma}} = \eta \bar{\mathbf{n}}_0^T \bar{\mathbf{P}}, \quad \mathbf{x} \in \Gamma(t), \quad \bar{\mathbf{x}} \in \bar{\Gamma}_0, \quad t > 0, \quad (12)$$

where  $\boldsymbol{\sigma} = -(p - p_e)I$  is the fluid stress with  $p_e$  defined as an equilibrium fluid pressure. The scale factor  $\eta$  in (12) is given in terms of  $\bar{\mathbf{F}}$  by Nanson's relation

$$\eta = \bar{J}^{-1} \mathbf{n}^T \bar{\mathbf{F}} \bar{\mathbf{n}}_0, \quad (13)$$

and it represents the ratio of an increment in surface area of the interface in the reference space to that in the physical space. Boundary conditions are required for the remainder of the fluid domain,  $\partial\Omega(t) \setminus \Gamma(t)$ , and for the remainder of the solid domain,  $\partial\bar{\Omega}_0 \setminus \bar{\Gamma}_0$ . These are chosen later depending on the problem under consideration. Finally, initial conditions for the fluid variables  $(\rho, \mathbf{v}, p)$  and the solid variables  $(\bar{\mathbf{u}}, \bar{\mathbf{v}}, p)$  are needed to complete the description of the initial-boundary-value FSI problem.

### 3. Fluid-solid Riemann problem and the AMP interface projection

The governing equations for the fluid in (1) and the solid in (6) are both hyperbolic systems of first-order equations. Each system possesses a characteristic structure which can be used to obtain a solution of a fluid-solid Riemann problem, described in this section for two space dimensions. The solution of this problem

forms the basis of the AMP projection step used in the DCG-FSI algorithm to obtain accurate and stable values of the state variables on the fluid-solid interface (see Section 4). For the purpose of this projection, we focus on finding values of the state variables on the interface from the solution to a fluid-solid Riemann problem.

### 3.1. Rotated equations

Figure 2 shows the geometry of the fluid-solid interface about a point  $Q$  in physical space. The equations for the fluid are given in the physical space  $\Omega(t)$  with interface denoted by  $\Gamma(t)$ , whereas the equations for the solid are described in a reference space  $\bar{\Omega}_0$  with interface denoted by  $\bar{\Gamma}_0$ . Let  $\mathbf{x}' = (x'_1, x'_2)$  denote orthogonal coordinates about the point  $Q$  with normal  $\mathbf{n}$ . Similarly,  $\bar{\mathbf{x}}' = (\bar{x}'_1, \bar{x}'_2)$  are orthogonal coordinates about the corresponding point  $\bar{Q}$  in the solid reference domain aligned with the outward normal  $\bar{\mathbf{n}}_0$ . The vectors  $\mathbf{t}$  and  $\bar{\mathbf{t}}_0$  denote unit vectors tangent to the interface at  $Q$  and  $\bar{Q}$ , respectively.

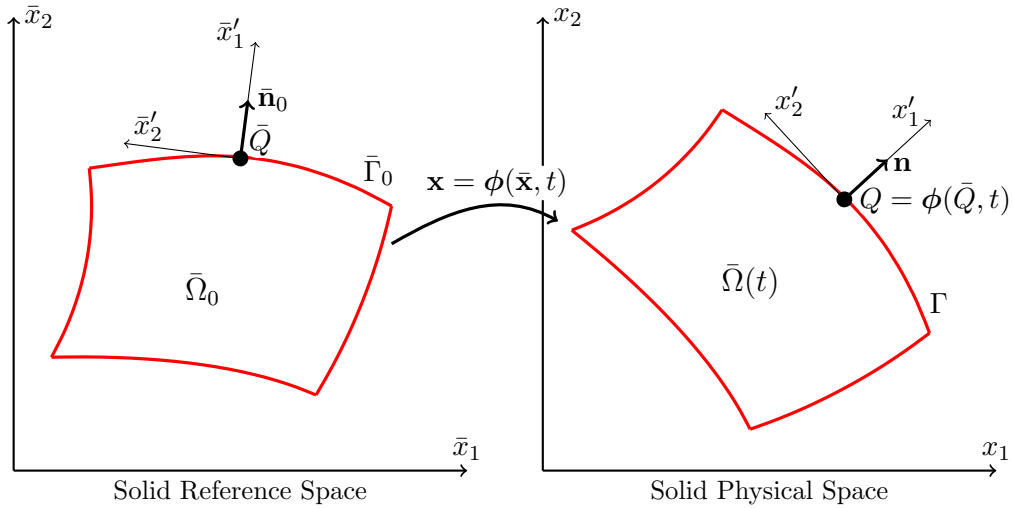


Figure 2: Left: Lagrangian solid reference domain with coordinates  $\bar{\mathbf{x}}$ . Right: Eulerian solid physical domain with coordinates  $\mathbf{x}$ . The rotated orthogonal coordinates  $(x'_1, x'_2)$  are aligned with the normal and tangent at point  $Q$  on the interface  $\Gamma$ .

The equations for the fluid and solid can be written in terms of their respective local coordinates. For the fluid-solid Riemann problem we are interested in the equations in the directions normal to the interface. For the fluid, the linearized equations are

$$\frac{\partial}{\partial t} \mathbf{q}' + A'_{1,0} \frac{\partial}{\partial x'_1} \mathbf{q}' = 0, \quad x'_1 > v'_{1,0} t, \quad t > 0, \quad (14)$$

where

$$\mathbf{q}' = \begin{bmatrix} \rho \\ v'_1 \\ v'_2 \\ p \end{bmatrix}, \quad A'_{1,0} = \begin{bmatrix} v'_{1,0} & \rho_0 & 0 & 0 \\ 0 & v'_{1,0} & 0 & 1/\rho_0 \\ 0 & 0 & v'_{1,0} & 0 \\ 0 & \rho_0 a_0^2 & 0 & v'_{1,0} \end{bmatrix}.$$

The components of the rotated fluid velocity in  $\mathbf{q}'$  are given by

$$v'_1 = \mathbf{n}^T \mathbf{v}, \quad v'_2 = \mathbf{t}^T \mathbf{v},$$

while  $v'_{1,0}$  and  $a_0 = \sqrt{\gamma p_0 / \rho_0}$  are the normal velocity and sound speed at  $Q$ , respectively. For the solid, the local equations are

$$\frac{\partial}{\partial t} \bar{\mathbf{q}}' + \bar{A}'_{1,0} \frac{\partial}{\partial \bar{x}'_1} \bar{\mathbf{q}}' = 0, \quad \bar{x}'_1 < 0, \quad t > 0, \quad (15)$$

where

$$\bar{\mathbf{q}}' = \begin{bmatrix} \bar{v}'_1 \\ \bar{v}'_2 \\ \bar{P}'_{11} \\ \bar{P}'_{12} \end{bmatrix}, \quad \bar{A}'_{1,0} = \begin{bmatrix} 0 & 0 & -1/\bar{\rho} & 0 \\ 0 & 0 & 0 & -1/\bar{\rho} \\ -\bar{T}'_{11} & -\bar{T}'_{12} & 0 & 0 \\ -\bar{T}'_{21} & -\bar{T}'_{22} & 0 & 0 \end{bmatrix}.$$

The components of the rotated solid velocity and stress in  $\bar{\mathbf{q}}'$  are given by

$$\bar{v}'_1 = \bar{\mathbf{n}}_0^T \bar{\mathbf{v}}, \quad \bar{v}'_2 = \bar{\mathbf{t}}_0^T \bar{\mathbf{v}}, \quad \bar{P}'_{11} = \bar{\mathbf{n}}_0^T \bar{P} \bar{\mathbf{n}}_0, \quad \bar{P}'_{12} = \bar{\mathbf{n}}_0^T \bar{P} \bar{\mathbf{t}}_0,$$

and the components of  $\bar{T}'$  are given by

$$\begin{aligned} \bar{T}'_{11} &= \bar{n}_{0,i} \bar{n}_{0,j} \bar{K}_{ijkl} \bar{n}_{0,k} \bar{n}_{0,\ell}, & \bar{T}'_{12} &= \bar{n}_{0,i} \bar{n}_{0,j} \bar{K}_{ijkl} \bar{t}_{0,k} \bar{n}_{0,\ell}, \\ \bar{T}'_{21} &= \bar{n}_{0,i} \bar{t}_{0,j} \bar{K}_{ijkl} \bar{n}_{0,k} \bar{n}_{0,\ell}, & \bar{T}'_{22} &= \bar{n}_{0,i} \bar{t}_{0,j} \bar{K}_{ijkl} \bar{t}_{0,k} \bar{n}_{0,\ell}, \end{aligned} \quad (16)$$

where  $\bar{K}_{ijkl}$  is evaluated at  $\bar{Q}$  and summation convention is assumed as before. The  $2 \times 2$  matrix  $\bar{T}'$  is symmetric in view of the major symmetry of  $\bar{K}_{ijkl}$  defined in (8), and we let  $\bar{\mathbf{y}}_p$  and  $\bar{\mathbf{y}}_s$  denote orthonormal left eigenvectors of  $\bar{T}'$  corresponding to its real eigenvalues  $\bar{\varphi}_p$  and  $\bar{\varphi}_s$ , respectively, assumed to satisfy  $0 < \bar{\varphi}_s < \bar{\varphi}_p$ . In the subsequent analysis, we let  $\bar{\mathbf{v}}' = (\bar{v}'_1, \bar{v}'_2)^T$  and  $\bar{\mathbf{w}}' = (\bar{P}'_{11}, \bar{P}'_{12})^T$ , and we note that the remaining two components of the rotated stress,  $\bar{P}'_{21}$  and  $\bar{P}'_{22}$ , decouple from the equations and are not needed in the analysis of the fluid-solid Riemann problem.

The characteristic form of the system of equations for the fluid in (14) gives

$$\begin{aligned} p \pm z_0 v_1 &= p_0 \pm z_0 v_{1,0} & \text{on } \frac{dx_1}{dt} &= v_{1,0} \pm a_0, \\ v_2 = v_{2,0}, \quad p - a_0^2 \rho &= p_0 - a_0^2 \rho_0 & \text{on } \frac{dx_1}{dt} &= v_{1,0}, \end{aligned} \quad (17)$$

where  $z_0 = \rho_0 a_0$  is the fluid impedance and the zero subscript denotes quantities evaluated at  $Q$ . (The primes have been dropped for notational convenience.) Similarly, the characteristic form of the system of equations for the solid in (15) gives

$$\begin{aligned} \bar{\mathbf{y}}_{p,0}^T \bar{\mathbf{w}} \mp \bar{z}_{p,0} \bar{\mathbf{y}}_{p,0}^T \bar{\mathbf{v}} &= \bar{\mathbf{y}}_{p,0}^T \bar{\mathbf{w}}_0 \mp \bar{z}_{p,0} \bar{\mathbf{y}}_{p,0}^T \bar{\mathbf{v}}_0 & \text{on } \frac{d\bar{x}_1}{dt} &= \pm \bar{c}_{p,0}, \\ \bar{\mathbf{y}}_{s,0}^T \bar{\mathbf{w}} \mp \bar{z}_{s,0} \bar{\mathbf{y}}_{s,0}^T \bar{\mathbf{v}} &= \bar{\mathbf{y}}_{s,0}^T \bar{\mathbf{w}}_0 \mp \bar{z}_{s,0} \bar{\mathbf{y}}_{s,0}^T \bar{\mathbf{v}}_0 & \text{on } \frac{d\bar{x}_1}{dt} &= \pm \bar{c}_{s,0}, \end{aligned} \quad (18)$$

where  $c_{p,0} = \sqrt{\bar{\varphi}_p/\bar{\rho}}$  and  $c_{s,0} = \sqrt{\bar{\varphi}_s/\bar{\rho}}$  are the characteristic velocities for p and s-waves, respectively, and  $z_{p,0} = \bar{\rho} c_{p,0}$  and  $z_{s,0} = \bar{\rho} c_{s,0}$  are solid impedances, all determined by the eigenvalues of  $\bar{T}$  evaluated at  $\bar{Q}$ .

### 3.2. AMP interface projections

We are now in a position to describe the states of the fluid and solid at the interface from the solution of the fluid-solid Riemann problem. Figure 3 provides some notation and illustrates the characteristic structure of the solution in the fluid and solid domains. We use the fluid equation

$$p^I - z_0 v_1^I = p_0 - z_0 v_{1,0}, \quad (19)$$

from (17) on the  $\mathcal{C}_-$  characteristic to give a relation between  $v_1^I$  and  $p^I$  on the interface, and the solid equations

$$\bar{\mathbf{y}}_{j,0}^T \bar{\mathbf{w}}^I - \bar{z}_{j,0} \bar{\mathbf{y}}_{j,0}^T \bar{\mathbf{v}}^I = \bar{\mathbf{y}}_{j,0}^T \bar{\mathbf{w}}_0 - \bar{z}_{j,0} \bar{\mathbf{y}}_{j,0}^T \bar{\mathbf{v}}_0, \quad j = p \text{ or } s, \quad (20)$$

from (18) on the  $\mathcal{C}_p$  and  $\mathcal{C}_s$  characteristics to give relations between the interface states  $\bar{\mathbf{v}}^I$  and  $\bar{\mathbf{w}}^I$ . The solution along the interface is then obtained by employing the matching conditions on velocity and stress.

To perform the matching along the interface, we must first describe the local velocity of the solid in terms of the local coordinates of the fluid. We must also rotate and scale the components of the nominal stress in  $\bar{\mathbf{w}}$  so that they may be matched with the stress (traction) of the fluid in the physical space given

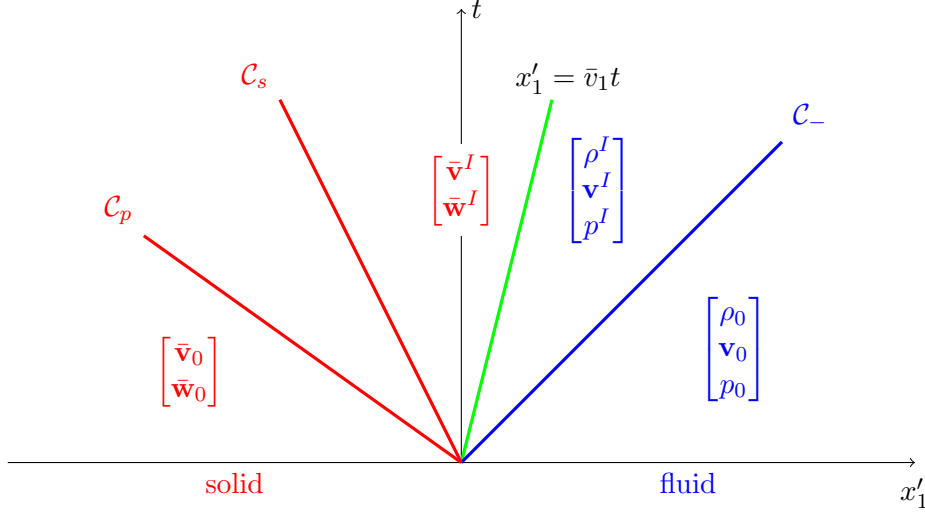


Figure 3: The  $x$ - $t$  diagram for the fluid-solid Riemann problem.

by  $\mathbf{w} = (p_e - p)\mathbf{n}$ . Let  $\hat{\mathbf{v}}$  and  $\hat{\mathbf{w}}$  denote the solid velocity and stress in the local fluid coordinates. These are given by

$$\hat{\mathbf{v}} = R\bar{\mathbf{v}}, \quad \hat{\mathbf{w}} = \eta R\bar{\mathbf{w}}, \quad (21)$$

where  $R$  is the rotation matrix defined by

$$R = \begin{bmatrix} \mathbf{n}^T \bar{\mathbf{n}}_0 & \mathbf{n}^T \bar{\mathbf{t}}_0 \\ \mathbf{t}^T \bar{\mathbf{n}}_0 & \mathbf{t}^T \bar{\mathbf{t}}_0 \end{bmatrix}, \quad (22)$$

and  $\eta$  is defined in (13). In terms of the rotated variables, the p-wave and s-wave characteristic relations in (20) become

$$\hat{\mathbf{y}}_{j,0}^T \hat{\mathbf{w}}^I - \hat{z}_{j,0} \hat{\mathbf{y}}_{j,0}^T \hat{\mathbf{v}}^I = \hat{\mathbf{y}}_{j,0}^T \hat{\mathbf{w}}_0 - \hat{z}_{j,0} \hat{\mathbf{y}}_{j,0}^T \hat{\mathbf{v}}_0, \quad j = p \text{ or } s, \quad (23)$$

where

$$\hat{\mathbf{y}}_{j,0} = R\bar{\mathbf{y}}_{j,0}, \quad \hat{z}_{j,0} = \eta \bar{z}_{j,0}, \quad j = p \text{ or } s.$$

The matching conditions on the normal component of velocity and on the normal and tangential components of stress are

$$\hat{v}_1^I = v_1^I, \quad \hat{w}_1^I = w_1^I, \quad \hat{w}_2^I = 0. \quad (24)$$

These conditions along with the characteristic relations for the fluid and solid in (19) and (23), respectively, can be used to obtain formulas for the normal components of the velocity and stress on the interface in terms of impedance-weighted averages of the local fluid and solid states at  $Q$  and  $\bar{Q}$ . We begin with the two characteristics equations in (23) and note that the orthonormal vectors  $\hat{\mathbf{y}}_{j,0}$ ,  $j = p$  or  $s$ , may be expressed as

$$\hat{\mathbf{y}}_{p,0} = (\cos \vartheta, \sin \vartheta)^T = (c, s)^T, \quad \hat{\mathbf{y}}_{s,0} = (-\sin \vartheta, \cos \vartheta)^T = (-s, c)^T, \quad (25)$$

where  $\vartheta$  is the angle between the rotated p-wave eigenvector  $\hat{\mathbf{y}}_{p,0}$  and the local fluid interface normal  $\mathbf{n}$ . Using (25) in (23) gives

$$\begin{aligned} c\hat{w}_1^I - \hat{z}_{p,0}(c\hat{v}_1^I + s\hat{v}_2^I) &= c\hat{w}_{1,0} + s\hat{w}_{2,0} - \hat{z}_{p,0}(c\hat{v}_{1,0} + s\hat{v}_{2,0}), \\ -s\hat{w}_1^I - \hat{z}_{s,0}(-s\hat{v}_1^I + c\hat{v}_2^I) &= -s\hat{w}_{1,0} + c\hat{w}_{2,0} - \hat{z}_{s,0}(-s\hat{v}_{1,0} + c\hat{v}_{2,0}), \end{aligned}$$

where we have used the matching condition  $\hat{w}_2^I = 0$ . Eliminating  $\hat{v}_2^I$  from these two equations gives

$$(c^2 \hat{z}_{s,0} + s^2 \hat{z}_{p,0})\hat{w}_1^I - \hat{z}_{p,0} \hat{z}_{s,0} \hat{v}_1^I = (c^2 \hat{z}_{s,0} + s^2 \hat{z}_{p,0})\hat{w}_{1,0} + sc(\hat{z}_{s,0} - \hat{z}_{p,0})\hat{w}_{2,0} - \hat{z}_{p,0} \hat{z}_{s,0} \hat{v}_{1,0},$$

which can be written in the compact form

$$\hat{w}_1^I - \hat{z}_0 \hat{v}_1^I = \hat{w}_{1,0} - \hat{k} \hat{w}_{2,0} - \hat{z}_0 \hat{v}_{1,0}, \quad (26)$$

where

$$\hat{z}_0 = \frac{\hat{z}_{p,0}\hat{z}_{s,0}}{c^2\hat{z}_{s,0} + s^2\hat{z}_{p,0}}, \quad \hat{k} = \frac{sc(\hat{z}_{p,0} - \hat{z}_{s,0})}{c^2\hat{z}_{s,0} + s^2\hat{z}_{p,0}}. \quad (27)$$

The characteristic equation for the fluid in (19), with  $w_1 = p_e - p$ , is

$$w_1^I + z_0 v_1^I = w_{1,0} + z_0 v_{1,0},$$

which can be used with (26) to give the interface states

$$\begin{aligned} \hat{v}_1^I = v_1^I &= \frac{\hat{z}_0 \hat{v}_{1,0} + z_0 v_{1,0}}{\hat{z}_0 + z_0} + \frac{w_{1,0} - \hat{w}_{1,0}}{\hat{z}_0 + z_0} + \frac{\hat{k} \hat{w}_{2,0}}{\hat{z}_0 + z_0}, \\ \hat{w}_1^I = w_1^I &= \frac{\hat{z}_0^{-1} \hat{w}_{1,0} + z_0^{-1} w_{1,0}}{\hat{z}_0^{-1} + z_0^{-1}} + \frac{v_{1,0} - \hat{v}_{1,0}}{\hat{z}_0^{-1} + z_0^{-1}} - \frac{\hat{z}_0^{-1} \hat{k} \hat{w}_{2,0}}{\hat{z}_0^{-1} + z_0^{-1}}. \end{aligned} \quad (28)$$

The formulas in (28) give the normal velocity and stress at the interface in terms of the velocity and stress in the fluid and solid on either side of the interface, and these can be used to determine the projected interface states in the AMP algorithm. We refer to the projection based on (28) as the *full AMP projection*.

The formulas in (28) can be simplified by noting that the tangential component of the traction stress,  $\hat{w}_2$ , is set to zero at the interface as a result of the interface matching conditions in (24), and thus this quantity is close to zero, on the order of the local truncation error, after each time step of the solid solver prior to enforcing  $\hat{w}_2^I = 0$ . This implies that  $\hat{w}_{2,0} \approx 0$  in (28), which gives

$$\begin{aligned} \hat{v}_1^I = v_1^I &= \frac{\bar{z}_p \hat{v}_{1,0} + z_0 v_{1,0}}{\bar{z}_p + z_0} + \frac{w_{1,0} - \hat{w}_{1,0}}{\bar{z}_p + z_0}, \\ \hat{w}_1^I = w_1^I &= \frac{\bar{z}_p^{-1} \hat{w}_{1,0} + z_0^{-1} w_{1,0}}{\bar{z}_p^{-1} + z_0^{-1}} + \frac{v_{1,0} - \hat{v}_{1,0}}{\bar{z}_p^{-1} + z_0^{-1}}. \end{aligned} \quad (29)$$

Here, we have made a further simplification by replacing  $\hat{z}_0$  with  $\bar{z}_p = \bar{\rho} c_p$ , where  $c_p = \sqrt{(\lambda + 2\bar{\mu})/\bar{\rho}}$ . This latter simplification is motivated by the observation that  $s \approx 0$  and  $\hat{z}_{p,0} \approx \bar{z}_p$ , and thus  $\hat{z}_0 \approx \bar{z}_p$  in (27), if the deformation gradient tensor is a small perturbation of a rotation matrix. The interface states given by (29) can also be used in the projection step of the AMP algorithm, which we refer to as the *simplified AMP projection*. We note that the formal order of accuracy of the FSI scheme is the same for either interface projection since the interface states given by (28) and (29) are both linear combinations of the original interface conditions, albeit with different weights. However, the simplified AMP projection is easier to implement and is less costly. The simplified projection could potentially lead to a less stable numerical scheme, although we have not found this to be the case at least for the FSI problems we have considered.

## 4. The FSI-DCG numerical approach for initial-boundary-value problems

Our numerical approach for the solution of the equations governing an FSI initial-boundary-value problem is based on the use of deforming composite grids (DCG). This FSI-DCG approach was described in [1] and employed for the case of an inviscid compressible flow coupled to a linearly elastic solid. The basic numerical approach is used here for FSI problems involving more general models of elastic solids; a summary of the approach is provided in Section 4.1 below. Further details are given in [1] and a more general discussion of overlapping grids can be found in [34–36], for example. Once the general DCG framework is described, we then discuss the numerical approximations for the equations governing the fluid and solid in Section 4.2. This is followed in Section 4.3 by a description of the time-stepping algorithm for the FSI initial-boundary-value problem.

### 4.1. Deforming composite grids

In the deforming-composite grid (DCG) approach for multi-domain problems, each fluid or solid domain is independently discretized with an overlapping grid. An overlapping grid,  $\mathcal{G}$ , consists of a set of structured component grids,  $\{G_g\}$ ,  $g = 1, \dots, \mathcal{N}$ , that cover a domain, either  $\Omega_k$  or  $\bar{\Omega}_k$ , and overlap where the component

grids meet. Typically, boundary-fitted curvilinear grids are used near the boundaries while one or more background Cartesian grids are used to handle the bulk of the domain. Each component grid is a logically rectangular, curvilinear grid in  $n_d$  space dimensions, and is defined by a smooth mapping from parameter space  $\mathbf{r}$  (the unit square or cube) to physical space  $\mathbf{x}$ ,

$$\mathbf{x} = \mathbf{g}(\mathbf{r}), \quad \mathbf{r} \in [0, 1]^{n_d}, \quad \mathbf{x} \in \mathbb{R}^{n_d}.$$

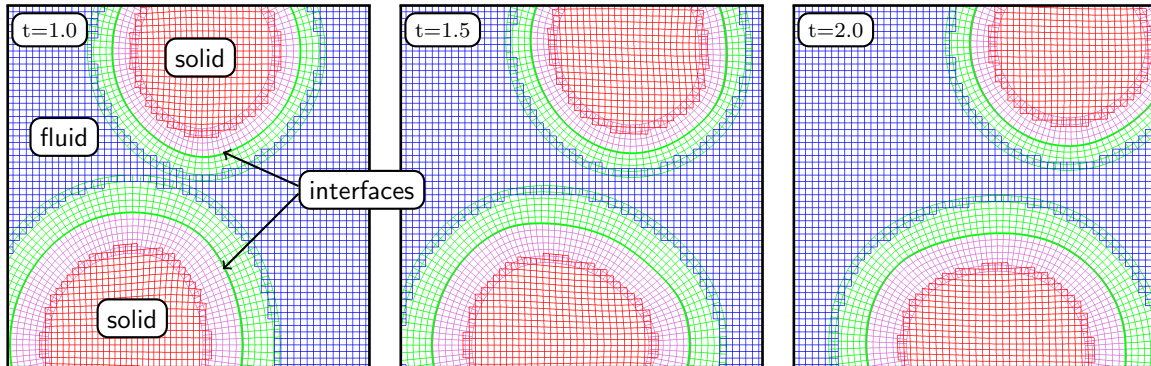


Figure 4: Composite grids at different times from the FSI-DCG simulation a shock hitting two solid elastic cylinders. The green fluid grids deform over time to follow the fluid-solid interfaces. The blue background Cartesian grid for the fluid remains fixed. The grids in the solid are shown adjusted for the displacements.

In the FSI-DCG approach, component grids next to an interface deform over time to match the interface motion. This is illustrated in Figure 4. After the points on the interfaces have been evolved from one time step to the next, a hyperbolic grid generator [37] is used to regenerate the interface grids. After the interface component grids are regenerated, the `Ogen` grid generator [38] is called to regenerate the overlapping grid connectivity (e.g., cut holes, determine interpolation points).

We use a strongly coupled partitioned approach to time step the numerical solutions on the fluid and solid domains. There is a separate fluid dynamics domain solver (`Cgcns`) for each fluid domain and a separate solid mechanics domain solver (`Cgsm`) for each solid domain. Thus, if there is one fluid domain and two solid domains (as in Figure 4), then there will be one instance of `Cgcns` and two instances of `Cgsm`. As a result of this separation, each fluid or solid in its respective domain may have independent material parameters and constitutive laws. A multi-physics control program (`Cgmp`) manages the multi-domain time stepping. At each time step, `Cgmp` calls the separate domain solvers to advance the solutions in their respective domains. `Cgmp` also manages the communication of interface data between the domain solvers and manages the assignment of the interface conditions.

#### 4.2. Discretization of the fluid and solid governing equations

The numerical approximation of the compressible Euler equations (1) follows the approach described in [7] for static grids and in [8] for moving rigid-body grids. Since this approximation has been discussed in detail elsewhere, we provide only a brief discussion of the discretization here. More details on the discretization of the solid equations are given below as these are new.

The first step in the numerical approach for either the fluid or solid equations involves an exact mapping of the equations from their respective domains of definition to computational space. For the Euler equations defined in the evolving domain  $\Omega(t)$ , consider a mapping for a (possibly moving) component grid given by  $\mathbf{x} = \mathbf{g}(\mathbf{r}, t)$ . Let

$$\dot{\mathbf{g}} = \frac{\partial \mathbf{g}}{\partial t},$$

denote the grid velocity vector with components  $\dot{g}_i$ . The conservative discretization of the governing equations on a mapped grid follows from the transformation for the divergence of a generic function  $\mathbf{h}$ , with

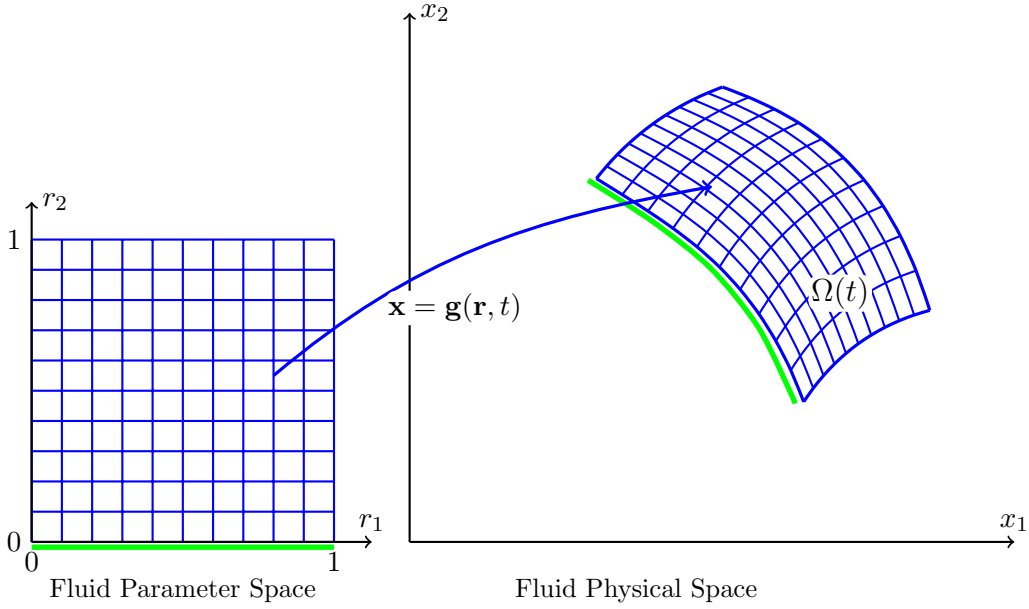


Figure 5: The fluid equations are discretized in the unit parameter space with coordinates  $\mathbf{r}$ , defined through the time-dependent mapping  $\bar{\mathbf{x}} = \mathbf{g}(\mathbf{r}, t)$  that defines the grid.

components  $h_i$ ,

$$\nabla \cdot \mathbf{h} = \frac{\partial h_j}{\partial x_j} = \frac{1}{J_g} \frac{\partial}{\partial r_k} \left( J_g \frac{\partial r_k}{\partial x_j} h_j \right), \quad (30)$$

where  $J_g$  is the Jacobian of the grid transformation,  $J_g = \det(\partial \mathbf{x} / \partial \mathbf{r})$ . Using (30) and following the work in [8], the mapped equations corresponding to (1) are

$$\frac{\partial q_i}{\partial t} + \frac{1}{J_g} \frac{\partial}{\partial r_k} \left( J_g \frac{\partial r_k}{\partial x_j} f_{ij} \right) - \frac{1}{J_g} \frac{\partial}{\partial r_k} \left( J_g \frac{\partial r_k}{\partial x_j} \dot{g}_j q_i \right) + \frac{q_i}{J_g} \frac{\partial}{\partial r_k} \left( J_g \frac{\partial r_k}{\partial x_j} \dot{g}_j \right) = 0. \quad (31)$$

The last two terms on the left-hand side of (31) arise from the moving coordinate transformation. The numerical approximation of the mapped Euler equations in (31) employ a second-order extension of Godunov's method. A Roe-type approximate Riemann solver is used to compute the mapped fluxes, but other Riemann solvers are also available. Slope-limited updates of the left and right input states to the Riemann solver are used to obtain second-order accuracy (for smooth regions of flow). Centered differences are used to approximate the (smooth) fourth term in (31) which describes the dilatation of a control volume in physical space as a result of the divergence of the grid velocity. The scheme is adjusted to ensure free-stream preservation, including the case of deforming grids. Further details, including a discussion of the numerical treatment of boundary conditions, may be found in [7] and [8].

For the solid we let  $\bar{\mathbf{x}} = \bar{\mathbf{g}}(\bar{\mathbf{r}})$  denote the static grid transformation from the coordinate  $\bar{\mathbf{r}}$  in parameter space to the reference coordinate  $\bar{\mathbf{x}} \in \bar{\Omega}_0$ . In parameter space, the system of equations in (4) becomes

$$\left. \begin{aligned} \frac{\partial \bar{u}_i}{\partial t} &= \bar{v}_i \\ \bar{\rho} \frac{\partial \bar{v}_i}{\partial t} &= \frac{1}{J_g} \frac{\partial \bar{f}_{i\alpha}}{\partial \bar{r}_\alpha} \\ \frac{\partial \bar{P}_{ij}}{\partial t} &= \tilde{K}_{ijk\alpha} \frac{\partial \bar{v}_k}{\partial \bar{r}_\alpha} \end{aligned} \right\}, \quad (32)$$

where  $\bar{f}_{i\alpha} = J_g(\partial \bar{r}_\alpha / \partial \bar{x}_j) \bar{P}_{ji}$  is a mapped flux of momentum in the  $\alpha$  coordinate direction and  $\tilde{K}_{ijk\alpha} = \bar{K}_{ijkl}(\partial \bar{r}_\alpha / \partial \bar{x}_\ell)$  is a mapped stress-strain tensor. This mapped tensor is a function of the deformation

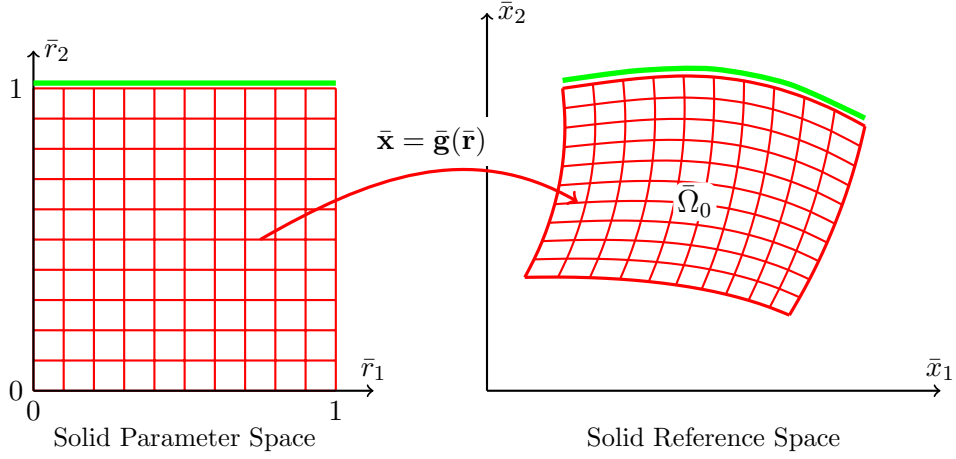


Figure 6: The solid equations are discretized in the unit parameter space with coordinates  $\bar{\mathbf{r}}$ , defined through the mapping  $\bar{\mathbf{x}} = \bar{\mathbf{g}}(\bar{\mathbf{r}})$  that defines the grid.

gradient tensor,  $\bar{F}$ , defined in (3), and whose components are given in terms of the mapped coordinates by

$$\bar{F}_{ij} = I_{ij} + \frac{\partial \bar{u}_i}{\partial \bar{r}_k} \frac{\partial \bar{r}_k}{\partial \bar{x}_j}. \quad (33)$$

We note that the system of equations in (4) and its mapped version in (32) involve hyperbolic equations in both conservative and nonconservative form. (The momentum equation for  $\bar{v}_i$  is in conservation form, while the equation for  $\bar{P}_{ij}$  is not.)

We discretize the mapped equations in (32) using a second-order (Godunov-based) upwind approach that can be considered as an extension of the one described in [9] for linearly elasticity. Here, however, the mapped equations for the solid are not based on a constant-coefficient set of equations, and are instead a mixed nonlinear conservative/nonconservative system of hyperbolic equations. To solve this mixed system, we use a numerical approach based on the ones discussed in [39] and [40]. The solution  $\bar{\mathbf{q}}_i^n$  for the solid at a time  $t^n$  is advanced in time on a two-dimensional Cartesian grid with coordinates  $\bar{\mathbf{r}}_i = (\bar{r}_{1,i}, \bar{r}_{2,i})$  in parameter space with mesh spacings  $\Delta \bar{r}_1$  and  $\Delta \bar{r}_2$ . (Here,  $\mathbf{i} = (i_1, i_2)$  is a multi-dimensional grid index.) The basic time-stepping scheme employs solutions of Riemann problems in each coordinate direction. Let  $\mathbf{e}_\alpha$  denote the unit index vector in the  $\alpha$  direction, i.e.  $\mathbf{e}_1 = (1, 0)$  and  $\mathbf{e}_2 = (0, 1)$  so that  $\mathbf{i} + \frac{1}{2}\mathbf{e}_1 = (i_1 + \frac{1}{2}, i_2)$  for example. The Riemann problem for  $\bar{v}_i(\bar{r}_1, t)$  and  $\bar{P}_{ij}(\bar{r}_1, t)$  in the  $\bar{r}_1$  direction centered about cell-face  $\bar{\mathbf{r}}_{\mathbf{i} + \frac{1}{2}\mathbf{e}_1}$  is then given by

$$\left. \begin{aligned} \rho \frac{\partial \bar{v}_i}{\partial t} &= \frac{1}{J_g} \frac{\partial \bar{f}_{i1}}{\partial \bar{r}_1} \\ \frac{\partial \bar{P}_{ij}}{\partial t} &= \tilde{K}_{ijk1} \frac{\partial \bar{v}_k}{\partial \bar{r}_1} \end{aligned} \right\}, \quad |\bar{r}_1| < \infty, \quad t > 0, \quad (34)$$

with initial data

$$\bar{v}_i(\bar{r}_1, 0) = \begin{cases} \bar{v}_i^L & \text{if } \bar{r}_1 < \bar{r}_{1, \mathbf{i} + \frac{1}{2}\mathbf{e}_1}, \\ \bar{v}_i^R & \text{if } \bar{r}_1 > \bar{r}_{1, \mathbf{i} + \frac{1}{2}\mathbf{e}_1}, \end{cases} \quad \bar{P}_{ij}(\bar{r}_1, 0) = \begin{cases} \bar{P}_{ij}^L & \text{if } \bar{r}_1 < \bar{r}_{1, \mathbf{i} + \frac{1}{2}\mathbf{e}_1}, \\ \bar{P}_{ij}^R & \text{if } \bar{r}_1 > \bar{r}_{1, \mathbf{i} + \frac{1}{2}\mathbf{e}_1}. \end{cases}$$

The left and right states for the velocity and nominal stress are obtained from values on the grid using left and right-biased slope-limited approximations to the solutions at  $\bar{r}_1 = \bar{r}_{1, \mathbf{i} + \frac{1}{2}\mathbf{e}_1}$  and  $t = t^n + \Delta t/2$  following the approach described in [9]. The stress-strain tensor  $\tilde{K}_{ijk1} = \tilde{K}_{ijk1}(\bar{F})$  is evaluated for a deformation gradient tensor,  $\bar{F}$ , obtained from (33) using central differences of a predicted displacement at  $t^n + \Delta t/2$  about  $\bar{\mathbf{r}}_{\mathbf{i} + \frac{1}{2}\mathbf{e}_1}$ , and held constant in the Riemann problem. The Jacobian of the mapping in (34) is evaluated at  $\bar{\mathbf{r}}_{\mathbf{i} + \frac{1}{2}\mathbf{e}_1}$ . The exact solution of this linearized Riemann problem (which is now a constant-coefficient system)

is obtained using the method of characteristics, and from this solution we extract the cell-face velocity and flux at  $\bar{\mathbf{r}}_{\mathbf{i}+\frac{1}{2}\mathbf{e}_1}$  and  $t^n + \Delta t/2$  denoted by  $\bar{v}_{\mathbf{i},\mathbf{i}+\frac{1}{2}\mathbf{e}_1}^{n+1/2}$  and  $\bar{f}_{\mathbf{i},\mathbf{i}+\frac{1}{2}\mathbf{e}_1}^{n+1/2}$ , respectively. A similar Riemann problem in the  $\bar{r}_2$  direction centered about  $\bar{\mathbf{r}}_{\mathbf{i}+\frac{1}{2}\mathbf{e}_2}$  yields  $\bar{v}_{\mathbf{i},\mathbf{i}+\frac{1}{2}\mathbf{e}_2}^{n+1/2}$  and  $\bar{f}_{\mathbf{i},\mathbf{i}+\frac{1}{2}\mathbf{e}_2}^{n+1/2}$ . The results of the Riemann problems are used to advance the velocity and stress to  $t^{n+1} = t^n + \Delta t$  according to the approximations

$$\frac{1}{\Delta t} \Delta_{+t} \bar{v}_{\mathbf{i},\mathbf{i}}^n = \frac{1}{\bar{\rho} J_{g,\mathbf{i}}} \sum_{\alpha=1}^{n_d} \frac{1}{\Delta \bar{r}_\alpha} \Delta_{+\alpha} \bar{f}_{\mathbf{i},\mathbf{i}-\frac{1}{2}\mathbf{e}_\alpha}^{n+1/2}, \quad (35)$$

and

$$\frac{1}{\Delta t} \Delta_{+t} \bar{P}_{ij,\mathbf{i}}^n = \sum_{\alpha=1}^{n_d} \frac{\tilde{K}_{ijk\alpha,\mathbf{i}}}{\Delta \bar{r}_\alpha} \Delta_{+\alpha} \bar{v}_{k,\mathbf{i}-\frac{1}{2}\mathbf{e}_\alpha}^{n+1/2} + \bar{\mathcal{D}}_{ij,\mathbf{i}}^P + \bar{\mathcal{R}}_{ij,\mathbf{i}}, \quad (36)$$

respectively. The operators  $\Delta_{+t}$  and  $\Delta_{+\alpha}$  are standard forward undivided difference operators in the  $t$  and  $\bar{r}_\alpha$  directions, respectively, defined by  $\Delta_{+t} h_{\mathbf{i}}^n = h_{\mathbf{i}}^{n+1} - h_{\mathbf{i}}^n$  and  $\Delta_{+\alpha} h_{\mathbf{i}}^n = h_{\mathbf{i}+\mathbf{e}_\alpha}^n - h_{\mathbf{i}}^n$ . The stress-strain tensor  $\tilde{K}_{ijk\alpha,\mathbf{i}} = \tilde{K}_{ijk\alpha}(\bar{F}_{\mathbf{i}}^{n+1/2})$  in (36) is obtained from the deformation gradient tensor using central differences of the predicted displacement at  $t^n + \Delta t/2$  centered at  $\bar{\mathbf{r}}_{\mathbf{i}}$ . The terms,  $\bar{\mathcal{D}}_{ij,\mathbf{i}}^P$  and  $\bar{\mathcal{R}}_{ij,\mathbf{i}}$ , appearing on the right-hand side of (36) are dissipation and relaxation terms, respectively, as described in more detail below. Finally, the displacement is advanced to  $t^{n+1}$  using

$$\frac{1}{\Delta t} \Delta_{+t} \bar{u}_{i,\mathbf{i}}^n = \bar{v}_{i,\mathbf{i}}^{n+1/2} + \bar{\mathcal{D}}_{i,\mathbf{i}}^u, \quad (37)$$

where  $\bar{v}_{i,\mathbf{i}}^{n+1/2}$  is a predicted velocity to  $t^n + \Delta t/2$  centered at  $\bar{\mathbf{r}}_{\mathbf{i}}$  and  $\bar{\mathcal{D}}_{i,\mathbf{i}}^u$  is a dissipation term as described below.

The approximations in (35), (36) and (37) provide the basic formulas to advance the velocity, stress and displacement in the solid from  $t^n$  to  $t^{n+1}$ . These are upwind approximations of the system of hyperbolic equations in (32). For a two-dimensional solid, this system has eight eigenvalues, four equal to the speeds of p- and s-waves in a chosen coordinate direction and four equal to zero. The characteristic variables for two of the four zero eigenvalues involve the components of the *tangential stress* given by  $\bar{t}_j^\alpha \bar{P}_{ji}$ , where  $\bar{t}_j^\alpha$  are components of the unit vector tangent to the coordinate face  $\bar{r}_\alpha = \text{constant}$ . The characteristic variables for the remaining two zero eigenvalues are the two components of displacement. The upwind approximations are effective in suppressing numerical oscillations in the characteristic variables corresponding to p- and s-waves (non-zero eigenvalues), but not effective in damping oscillations in the components of the tangential stress and in the displacement which are neutrally stable. For these latter components, we find it necessary to add numerical dissipation to the approximations to suppress possible weak instabilities at grid overlaps (see [9] for a further discussion). The dissipation is defined in terms of the  $m^{\text{th}}$ -order dissipation operator given by

$$\mathcal{D}_\alpha^{(m)} = \frac{1}{2^m} \left( -\Delta_{+\alpha} \Delta_{-\alpha} \right)^{m/2}, \quad (38)$$

where  $\Delta_{-\alpha}$  is defined by  $\Delta_{-\alpha} h_{\mathbf{i}} = h_{\mathbf{i}} - h_{\mathbf{i}-\mathbf{e}_\alpha}$  and  $\Delta_{+\alpha}$  was defined above. The factor  $1/2^m$  is included to normalize the dissipation operator so that for a periodic problem the discrete  $L_2$ -norm of  $\mathcal{D}_\alpha^{(m)}$  is equal to one (see [41]). The dissipation operator in (38) is chosen because it is effective at filtering high-frequency numerical oscillations. To suppress oscillations in the tangential components of stress, we add the fourth-order ( $m = 4$ ) dissipation term,

$$\bar{\mathcal{D}}_{ij,\mathbf{i}}^P = -\frac{\bar{\beta}^P}{\Delta t} \left[ \frac{1}{n_d} \sum_{\alpha=1}^{n_d} \bar{t}_{i,\mathbf{i}}^\alpha \bar{t}_{k,\mathbf{i}}^\alpha \mathcal{D}_\alpha^{(4)} \bar{P}_{kj,\mathbf{i}}^n \right], \quad (39)$$

to the right-hand side of the equation (36) for  $\bar{P}_{ij,\mathbf{i}}^{n+1}$ . Here,  $\bar{\beta}^P$  is a dissipation coefficient that is typically taken to be  $\frac{1}{2}$ . For smooth solutions, the dissipation adds an  $\mathcal{O}(\Delta \bar{r}_\alpha^4 / \Delta t) = \mathcal{O}(\Delta \bar{r}_\alpha^3)$  contribution to (36) which is below the level of the second-order truncation error  $\mathcal{O}(\Delta \bar{r}_\alpha^2)$ . For the displacement, we add a similar fourth-order dissipation term,

$$\bar{\mathcal{D}}_{i,\mathbf{i}}^u = -\frac{\bar{\beta}^u}{\Delta t} \left[ \frac{1}{n_d} \sum_{\alpha=1}^{n_d} \mathcal{D}_\alpha^{(4)} \bar{u}_{i,\mathbf{i}}^n \right], \quad (40)$$

to the right-hand side of (37), where  $\bar{\beta}^u$  is a dissipation coefficient. Note that the factor of  $1/\Delta t$  in (39) and (40) is included so that the dissipation coefficients  $\bar{\beta}^P$  and  $\bar{\beta}^u$  are dimensionless.

Finally, we add a stress-strain relaxation term to the right-hand side of (36) to help ensure that the stress-strain relation remains nearly satisfied in the discrete solution even for long-time integrations. The relaxation term is similar to the one used in [1] and is given by

$$\bar{\mathcal{R}}_{ij,i} = -\frac{\bar{\beta}^r}{\Delta t} \left[ \bar{P}_{ij,i}^n - \bar{\mathcal{P}}_{ij}(\bar{F}_{ij,i}^n) \right], \quad (41)$$

where  $\bar{\beta}^r$  is a dimensionless constant,  $\bar{\mathcal{P}}_{ij}(\bar{F}_{ij})$  is the stress-strain constitutive relation, and  $\bar{F}_{ij,i}^n$  is an approximation of the deformation gradient tensor computed using fourth-order accurate central differences of the displacement. The relaxation term in (41) adds an  $\mathcal{O}(\Delta \bar{r}_\alpha^4/\Delta t)$  contribution to (36) when  $\bar{\beta}^r$  is  $\mathcal{O}(1)$ . In general, we observe that the numerical errors in the components of stress are reduced when stress-strain relaxation is used. We note that the numerical approximation for the nonlinear elasticity equations is adjusted to ensure free-stream preservation, as done in [9], and that the overall FSI-DCG approximation is also free-stream preserving.

*Boundary conditions for the solid.* The boundary conditions for the solid domain  $\bar{\Omega}_0$  away from the fluid-solid interface on  $\partial\bar{\Omega}_0 \setminus \bar{\Gamma}_0$  may be of *displacement*, *traction* or *slip-wall* type. The numerical treatment of these boundary conditions for the case of linear elasticity was discussed in [9], and we follow a similar approach for the nonlinear equations here. The principal difference in the numerical application of the boundary conditions, and the associated compatibility conditions, concerns the approximation of the deformation gradient tensor,  $\bar{F}$ , on the boundary. Let us consider, for example, the case of traction boundary conditions for which

$$\boldsymbol{\tau}_b = \mathbf{n}^T \bar{\boldsymbol{\sigma}} = \eta \bar{\mathbf{n}}_0^T \bar{P}, \quad \bar{\mathbf{x}} \in \partial\bar{\Omega}_0^{\bar{\boldsymbol{\sigma}}}, \quad (42)$$

where  $\boldsymbol{\tau}_b$  is the given traction on the boundary  $\partial\bar{\Omega}_0^{\bar{\boldsymbol{\sigma}}}$  and  $\eta$  is given by (13). The boundary condition in (42) is a *primary* condition for the normal components of the nominal stress,  $\bar{P}$ , whereas *secondary* compatibility conditions are used to specify values of the solution on ghost points as well as the tangential components of stress on the boundary. To obtain values of the displacement on ghost points, we use the compatibility condition

$$\bar{\mathbf{n}}_0^T \bar{P} = \bar{\mathbf{n}}_0^T \bar{\mathcal{P}}(\bar{F}), \quad \bar{\mathbf{x}} \in \partial\bar{\Gamma}_0^{\bar{\boldsymbol{\sigma}}}, \quad (43)$$

where  $\bar{F} = I + \nabla_{\bar{\mathbf{x}}} \bar{\mathbf{u}}$  is approximated on the grid using standard second-order central differences. These approximations involve differences of  $\bar{\mathbf{u}}$  in the normal and tangential directions to the boundary. Central differences of  $\bar{\mathbf{u}}$  in the tangential direction can be computed using existing values on the boundary of the grid. Thus, the two components of (43) are regarded as equations for the two components of  $\bar{\mathbf{n}}_0^T \nabla_{\bar{\mathbf{x}}} \bar{\mathbf{u}}$ , which then specifies discrete values for  $\bar{\mathbf{u}}$  at ghost points. The equations in (43) for  $\bar{F}$  are nonlinear, in general, and are solved using Newton's method. Discrete values for the velocity at ghost points are obtained by considering the time derivative of (43), while  $\bar{\mathbf{t}}_0^T \bar{P} = \bar{\mathbf{t}}_0^T \bar{\mathcal{P}}(\bar{F})$  is used to set discrete values for the tangential components of stress on the boundary of the grid (using the computed approximation of  $\bar{F}$ ).

*Time step determination.* The choice of the time step,  $\Delta t$ , for the fluid and solid solvers independently has been discussed in [7] and [9], respectively, and ultimately it is the minimum of these time steps that is used for the FSI-DCG time-stepping algorithm described below. There is no restriction on the time step imposed by the interface projection scheme. Some modifications to the previous time-step formulas are needed, however, to treat the dissipation terms in (39) and (40) which are new, as well as the stress-strain relaxation term in (41), since these are proportional to  $1/\Delta t$ . The time step  $\Delta t$  is determined from the *time-stepping eigenvalue* for the discrete approximation based on a generalized von Neumann stability analysis. The time-stepping eigenvalue (or Fourier *symbol* of the discrete operator) is of the form

$$\Lambda = \Lambda_r + i\Lambda_i - \frac{\beta}{\Delta t}, \quad (44)$$

where  $\Lambda_r$  and  $\Lambda_i$  are real constants that depend on the grid spacing and other parameters (e.g.  $\Lambda_i = \bar{c}_p(1/\Delta x_1 + 1/\Delta x_2)$  for a linear elastic solid on a two-dimensional Cartesian grid) and where

$\beta = \max(\bar{\beta}^u, \bar{\beta}^P, \bar{\beta}^r)$ . Given values for  $\beta$ ,  $\Lambda_r$  and  $\Lambda_i$ , an estimate for the maximal allowable time step is determined from the condition

$$\left[ \frac{(\Lambda_r - \frac{\beta}{\Delta t})\Delta t}{\ell_r} \right]^2 + \left[ \frac{\Lambda_i \Delta t}{\ell_i} \right]^2 \leq 1. \quad (45)$$

Here the region of absolute stability of the scheme has been approximated by the interior of the ellipse with boundary  $(\text{Re}(\Lambda)\Delta t/\ell_r)^2 + (\text{Im}(\Lambda)\Delta t/\ell_i)^2 = 1$ . The lengths,  $\ell_r$  and  $\ell_i$ , of the semi-axes of the ellipse are chosen based on the particular time-stepping scheme used as discussed in [7] and [9]. Here, we use  $\ell_r = 2$  and  $\ell_i = 1$ . The maximum value of the time step implied by the inequality in (45), which is quadratic in  $\Delta t$ , is given by

$$\Delta t_{\max} = \frac{-b + \sqrt{b^2 - 4ac}}{2a},$$

where

$$a = \left( \frac{\Lambda_r}{\ell_r} \right)^2 + \left( \frac{\Lambda_i}{\ell_i} \right)^2, \quad b = -2 \frac{\Lambda_r \beta}{\ell_r^2}, \quad c = \left( \frac{\beta}{\ell_r} \right)^2 - 1.$$

The time step is not significantly impacted by the addition of the dissipation terms and the stress relaxation provided  $\beta/\ell_r$  is not too large. In practice, the time step is further multiplied by a *safety factor*  $C_{\text{CFL}}$ , typically taken to be 0.9.

#### 4.3. FSI-DCG time-stepping algorithm with AMP projection

---

**Procedure 1** The basic FSI-DCG time-stepping algorithm.

---

```

1: procedure SOLVEFSIDCG( $\mathcal{G}$ ,  $t_{\text{final}}$ )                                ▷ Input: initial composite grid and final time
2:    $t := 0$ ;  $n := 0$ ;  $\mathcal{G}^n = \mathcal{G}$ ;
3:   assignInitialConditions( $\mathbf{q}_i^n$ ,  $\bar{\mathbf{q}}_i^n$ ,  $\mathcal{G}^n$ );
4:   while  $t < t_{\text{final}}$  do
5:      $\Delta t := \text{computeTimeStep}(\mathbf{q}_i^n, \bar{\mathbf{q}}_i^n, \mathcal{G}^n)$ ;
6:      $\mathcal{G}^p := \text{moveGrids}(\mathcal{G}^n, \mathbf{q}_i^n, \bar{\mathbf{q}}_i^n)$ ;                                ▷ Generate new interface grids
7:      $\mathcal{G}^p := \text{updateOverlappingGrid}(\mathcal{G}^p)$ ;                                ▷ Update overlapping grid connectivity
8:      $\mathbf{q}_i^{n+1} := \text{advanceFluid}(\mathbf{q}_i^n, \mathcal{G}^p, \mathcal{G}^p, \Delta t)$ ;                                ▷ Advance fluid
9:      $\bar{\mathbf{q}}_i^{n+1} := \text{advanceSolid}(\bar{\mathbf{q}}_i^n, \mathcal{G}, \Delta t)$ ;                                ▷ Advance solid
10:     $(\mathbf{n}^T \mathbf{v}^I, \mathbf{n}^T \boldsymbol{\sigma}^I) := \text{projectInterface}(\mathbf{q}_i^{n+1}, \bar{\mathbf{q}}_i^{n+1}, \mathcal{G}^p)$ ;                                ▷ Project interface
11:     $\mathbf{q}_i^{n+1} := \text{applyFluidBCs}(\mathbf{q}_i^{n+1}, \mathcal{G}^p, \mathbf{n}^T \mathbf{v}^I, \mathbf{n}^T \boldsymbol{\sigma}^I)$ ;                                ▷ Assign fluid BCs
12:     $\bar{\mathbf{q}}_i^{n+1} := \text{applySolidBCs}(\bar{\mathbf{q}}_i^{n+1}, \mathcal{G}, \mathbf{n}^T \mathbf{v}^I, \mathbf{n}^T \boldsymbol{\sigma}^I)$ ;                                ▷ Assign solid BCs
13:     $\mathcal{G}^{n+1} := \text{correctMovingGrids}(\mathbf{q}_i^{n+1}, \bar{\mathbf{q}}_i^{n+1}, \mathcal{G}^p, \Delta t)$ ;                                ▷ Correct moving grids
14:     $t := t + \Delta t$ ;  $n := n + 1$ ;
15:   end while
16: end procedure

```

---

The FSI-DCG time-stepping algorithm is outlined in Procedure 1. The initial grids for the fluid and solid domains, denoted collectively by  $\mathcal{G}$ , are constructed in a pre-processing step using the *Ogen* grid generator [38]. The algorithm starts by assigning initial conditions for the fluid state,  $\mathbf{q}_i^0$ , and the solid state,  $\bar{\mathbf{q}}_i^0$ , on  $\mathcal{G}$ . At the beginning of the time-stepping loop, a stable global value for the time step increment  $\Delta t$  is computed as described in Section 4.2. A predicted version of the new fluid grid at  $t + \Delta t$  is constructed by moving the interface according to the solution at  $t$  and regenerating the boundary-fitted grid next to the interface using the hyperbolic grid generator [37]. The overlapping grid is then regenerated by *Ogen* (performing *hole cutting* and determination of interpolation points). Given the (predicted) grid at the new time,  $\mathcal{G}^p$ , the state of the fluid is advanced to obtain predicted values for the fluid state,  $\mathbf{q}_i^p$ , at time  $t^{n+1}$ . No boundary conditions are applied on the interface at this stage, although predicted values on the interface are

determined since the equations are applied on the interface points with the aid of ghost points. Similarly the solid state is advanced to obtain predicted values,  $\bar{\mathbf{q}}_i^p$ , at the new time  $t^{n+1}$  and, as for the fluid, no boundary conditions on the interface are applied. Given predicted values for the fluid and solid interface velocity and traction, the actual interface values are computed, based on the fluid-solid Riemann problem, using the AMP interface projection described in Section 3. Typically, we use the simplified interface projection given by (29) and as we discuss further in Section 6. With projected interface values for the fluid velocity and traction, the boundary conditions on the fluid and solid domains are assigned. The final step in the loop involves updating the interface grids to reflect the corrected position of the interface.

*A note on interface boundary conditions.* In our previous paper that described an AMP-algorithm for inviscid compressible fluid interacting with a linearly-elastic solid [1], we developed special interface compatibility conditions to assign the values of the discrete solution on ghost points adjacent to the interface. Although this technique worked well, it is more convenient in practice to make use of the existing infrastructure for assigning boundary values and ghost values available with the separate fluid and solid solvers. In this paper we take this latter approach. We assign ghost values on the interface in the fluid domain using the compatibility conditions associated with a moving slip wall. We assign ghost values on the interface in the solid domain using the compatibility conditions associated with a moving traction wall. The ghost values (but *not* the interface values, which are obtained from the projection) are thus assigned following the strategy associated with the traditional partitioned algorithm. This approach makes it easier to incorporate the interface projection into existing partitioned solvers.

## 5. Convergence tests

In this section, we describe results of two tests of the AMP algorithm. The first test uses the method of analytic solutions for an elastic piston problem. In this test, forcing functions are added to the governing equations for the fluid and solid (and to the boundary and interface conditions) so that an exact solution is known. Numerical solutions are computed on a sequence of grids and max-norm errors are evaluated to verify second-order accuracy of the algorithm. In the second test, we consider an FSI problem involving a rotating elastic disk immersed in an inviscid compressible fluid. An analysis of the problem assuming circular symmetry leads to a reduced set of governing equations which are solved numerically on a very fine one-dimensional grid in the radial direction. This solution is treated as an exact solution and used to verify the accuracy and stability of the AMP algorithm for heavy, medium and light solids.

### 5.1. The method of analytic solutions

The method of analytic solutions is a useful technique for constructing exact solutions of initial-boundary-value problems for partial differential equations for the purpose of checking the behavior and accuracy of the numerical implementation of a problem. This method, also known as the *method of manufactured solutions* [42] or *twilight-zone forcing* [36], adds forcing functions to the governing equations, boundary conditions and interface conditions. These forcing functions are specified so that a chosen function,  $\tilde{\mathbf{q}}(\mathbf{x}, t)$ , becomes the exact solution of the forced equations, and thus the error in the discrete solution can be computed exactly.

In the results presented below, the method of analytic solutions is applied using solutions given in terms of trigonometric functions. In particular, the exact solutions for the components of displacement, velocity and stress in the solid are taken to be

$$\begin{aligned} \tilde{u}_1 &= .25 \alpha \bar{c}_1 \tilde{c}_2 c_t, & \tilde{u}_2 &= .5 \alpha \bar{c}_1 \tilde{c}_2 c_t, & \tilde{P}_{11} &= -.5 \alpha \bar{c}_1 \tilde{c}_2 c_t, & \tilde{P}_{12} &= .4 \alpha \bar{s}_1 \tilde{c}_2 c_t, \\ \tilde{v}_1 &= \dot{u}_1, & \tilde{v}_2 &= \dot{u}_2, & \tilde{P}_{21} &= .4 \alpha \bar{s}_1 \tilde{c}_2 c_t, & \tilde{P}_{22} &= .6 \alpha \bar{c}_1 \bar{s}_2 c_t \end{aligned} \quad (46)$$

where  $(\bar{c}_1, \bar{s}_1) = (\cos(2\pi\bar{x}_1), \sin(2\pi\bar{x}_1))$ ,  $(\bar{c}_2, \bar{s}_2) = (\cos(2\pi\bar{x}_2), \sin(2\pi\bar{x}_2))$ ,  $\tilde{c}_2 = \cos(2\pi(\bar{x}_2 + 0.375))$ ,  $c_t = \cos(2\pi t)$  and where  $\alpha$  is a scale factor. We choose the SVK constitutive model given in (9) with  $\bar{\lambda} = \bar{\mu} = 0.1$ . We take  $\bar{\rho} = 0.1$  for the density of the solid in the reference configuration, and choose  $\alpha = 10^{-2}$  to ensure that the deformation gradient determined by the manufactured solution is sufficiently close to the identity

so that the governing equations for the solid remain hyperbolic. The exact solutions for the density, velocity and pressure in the fluid are chosen to be

$$\tilde{\rho} = \alpha (1 + .125s_1c_2c_t), \quad \tilde{v}_1 = .5\alpha c_1c_2c_t, \quad \tilde{v}_2 = .5\alpha s_1s_2c_t, \quad \tilde{p} = \alpha c_1s_2c_t, \quad (47)$$

where  $(c_1, s_1) = (\cos(2\pi x_1), \sin(2\pi x_1))$  and  $(c_2, s_2) = (\cos(2\pi x_2), \sin(2\pi x_2))$ . The ratio of specific heats in the fluid is taken to be  $\gamma = 1.4$ .

An initial-boundary-value problem is defined for the geometry associated with the *elastic piston* test problem used in [1], see Figure 7. The geometry of the problem consists of a solid reference domain on  $[-1, 0] \times [0, 1]$  and a fluid domain initially on  $[0, 1.5] \times [0, 1]$ . Initial conditions for the problem are taken from the exact solutions in (46) and (47) for the solid and fluid in their respective domains. The boundary conditions on the top and bottom faces of the solid and fluid are taken as symmetry conditions, with a suitable forcing derived from the exact solution, and Dirichlet boundary conditions are taken from the exact solutions and applied on the left face of the solid and the right face of the fluid. The matching conditions on the interface between the solid and fluid domains are specified, with appropriate forcing functions, on a vertical boundary with a given horizontal motion taken to be  $x_1 = Vt$ , where  $V = 0.5$ .

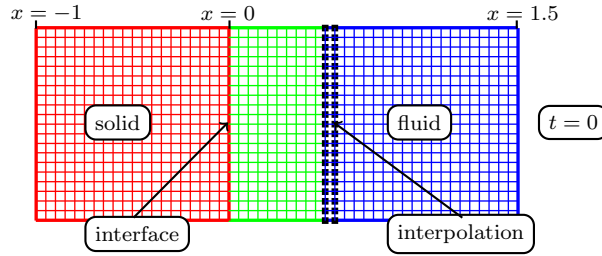


Figure 7: The composite grid  $\mathcal{G}_{ep}^{(2)}$  for the two-dimensional elastic piston problem at time  $t = 0$ . The fluid domain is covered by a blue background grid and green grid that follows the interface. The solid domain is represented with the red grid.

Numerical solutions are computed using the AMP algorithm on deforming composite grids with increasing resolution. Let  $\mathcal{G}_{ep}^{(j)}$  denote the composite grid for the problem with grid spacings  $\Delta x_1^{(j)} = \Delta x_2^{(j)} = 1/(10j)$  in the solid and fluid domains so that the index  $j$  determines the grid resolution. Figure 7 illustrates the composite grid at  $t = 0$  for the case  $j = 2$ . The composite grid consists of a static rectangular grid  $\mathcal{R}_s$  for the solid domain  $[-1, 0] \times [0, 1]$ , a static background rectangular grid  $\mathcal{R}_f$  on  $[-.75, 1.5] \times [0, 1]$  for the fluid along with a deforming hyperbolic grid of normal width 0.5 next to the interface. The fluid domain is thus represented by the hyperbolic grid and the background grid which overlap where they meet. At each time step, the fluid interface moves with the specified velocity  $V$ , and the hyperbolic grid generator is called to regenerate the deforming grid near the fluid interface. We note that the FSI problem with solution constructed using the method of analytic solutions provides a good check of the order of accuracy of the numerical approach, but it does not fully assess the stability of scheme since the interface motion is specified. The accuracy and stability of the AMP algorithm for heavy, medium and light solid is checked in the next test problem.

The table in Figure 8 shows the maximum errors in the components of the numerical solutions computed on the composite grid  $\mathcal{G}_{ep}^{(j)}$  for  $j = 2, \dots, 5$  using the AMP algorithm with simplified interface projection defined in Section 3.2. The columns labeled  $E_j^{(q)}$  give the maximum errors for solution component  $q$  at time  $t = 0.5$ . For vector variables, such as  $\bar{v}$  or  $\bar{P}$ , the errors denote the maximum over all components of the vector or tensor. The errors for the fluid component labeled  $T$  is given by the ratio  $p/\rho$ . The columns labeled  $r$  give the ratio of successive errors, which should be approximately equal to 4 for second-order accuracy. The convergence rate,  $\zeta_q$ , for component  $q$  is estimated by a least squares fit to the logarithm of the error equation,  $E_j^{(q)} = C_q h_j^{\zeta_q}$ , where  $C_q$  is assumed to be approximately constant for small grid spacings. These rates show that the AMP algorithm is close to second-order accurate in the maximum norm.

Manufactured Solutions, SVK Elastic Piston														
$h_j$	$E_j^{(\rho)}$	$r$	$E_j^{(v_1)}$	$r$	$E_j^{(v_2)}$	$r$	$E_j^{(T)}$	$r$	$E_j^{(\bar{u})}$	$r$	$E_j^{(\bar{v})}$	$r$	$E_j^{(\bar{P})}$	$r$
1/20	1.8e-5		6.9e-4		9.4e-5		1.1e-4		1.2e-4		6.9e-4		9.7e-5	
1/40	4.8e-6	3.7	1.7e-4	4.0	2.3e-5	4.1	3.4e-5	3.2	3.3e-5	3.6	1.7e-4	4.0	2.4e-5	4.1
1/80	1.2e-6	3.9	4.3e-5	4.0	5.1e-6	4.4	8.9e-6	3.8	8.7e-6	3.8	4.3e-5	4.0	5.9e-6	4.0
1/160	3.1e-7	4.0	1.1e-5	4.0	1.2e-6	4.2	2.3e-6	3.9	2.2e-6	3.9	1.1e-5	4.0	1.5e-6	4.0
rate	1.95		2.01		2.10		1.87		1.91		2.00		2.02	

Figure 8: FSI-AMP algorithm, manufactured solutions, SVK elastic piston. Maximum errors and estimated convergence rates at  $t = 0.5$ .

## 5.2. Rotating disk

As a second test of the AMP algorithm, we consider a model FSI problem consisting of a solid disk in the reference domain  $\bar{\Omega}_0 = \{(\bar{x}_1, \bar{x}_2) \mid \bar{x}_1^2 + \bar{x}_2^2 < 1\}$  coupled to a fluid initially at rest in the annular domain  $\Omega(0) = \{(x_1, x_2) \mid 1 < x_1^2 + x_2^2 < b^2\}$ ,  $b > 1$ , surrounding the solid. The solid is set into motion by an initial angular velocity, and the fluid responds as a result of the radial displacement of the fluid-solid interface. In effect, the rotating solid generates a radially oscillating fluid-solid interface that acts as a radial piston for the fluid. The solution of the FSI problem is circularly symmetric and depends only on radial position, both in the reference space of the solid and in the physical space of the fluid, and time. The AMP algorithm can be used to compute solutions of the rotating disk problem without assuming any symmetry, and then compared with a fine-grid solution<sup>6</sup> of the reduced one-dimensional equations which exploit the circular symmetry of the problem. This comparison is done for heavy, medium and light solids to verify the accuracy and stability of the algorithm.

We begin by considering the reduced equations for the FSI problem assuming circular symmetry. For this reduction, the first-order equations in (1) governing the fluid are written in terms of the polar coordinates  $(r, \theta)$  in physical space defined by  $x_1 = r \cos \theta$  and  $x_2 = r \sin \theta$ . The equations are then reduced assuming that all dependent variables depend on  $r$  and  $t$  alone. The resulting equations are

$$\frac{\partial}{\partial t} \begin{bmatrix} \rho \\ \rho v_r \\ \rho E \end{bmatrix} + \frac{\partial}{\partial r} \begin{bmatrix} \rho v_r \\ \rho v_r^2 + p \\ v_r(\rho E + p) \end{bmatrix} + \frac{v_r}{r} \begin{bmatrix} \rho \\ \rho v_r \\ \rho E + p \end{bmatrix} = 0, \quad (48)$$

where  $v_r$  is the component of the fluid velocity in the  $r$  direction while the component of velocity in the  $\theta$  direction is assumed to be zero.

For the solid, the second-order form of the governing equations in (2) become

$$\bar{\rho} \frac{\partial^2}{\partial \bar{t}^2} \bar{u}_j = \frac{1}{\bar{r}} \frac{\partial}{\partial \bar{r}} (\bar{r}(\bar{P}_{1j} \cos \bar{\theta} + \bar{P}_{2j} \sin \bar{\theta})) + \frac{1}{\bar{r}} \frac{\partial}{\partial \bar{\theta}} (-\bar{P}_{1j} \sin \bar{\theta} + \bar{P}_{2j} \cos \bar{\theta}), \quad j = 1, 2, \quad (49)$$

in terms of the polar coordinates  $(\bar{r}, \bar{\theta})$  defined by  $\bar{x}_1 = \bar{r} \cos \bar{\theta}$  and  $\bar{x}_2 = \bar{r} \sin \bar{\theta}$ . We consider radial and angular displacements,  $\bar{u}_r$  and  $\bar{u}_\theta$ , defined by

$$x_1 = \bar{x}_1 + \bar{u}_1 = (\bar{r} + \bar{u}_r) \cos(\bar{\theta} + \bar{u}_\theta), \quad x_2 = \bar{x}_2 + \bar{u}_2 = (\bar{r} + \bar{u}_r) \sin(\bar{\theta} + \bar{u}_\theta).$$

In terms of these displacements and assuming that  $\bar{u}_r = \bar{u}_r(\bar{r}, t)$  and  $\bar{u}_\theta = \bar{u}_\theta(\bar{r}, t)$ , the governing equations in (49) reduce to

$$\begin{aligned} \bar{\rho} \left\{ \frac{\partial^2 \bar{u}_r}{\partial \bar{t}^2} - (\bar{r} + \bar{u}_r) \left( \frac{\partial \bar{u}_\theta}{\partial \bar{t}} \right)^2 \right\} &= \frac{1}{\bar{r}} \left[ \frac{\partial}{\partial \bar{r}} (\bar{r} \tilde{P}_{11}) - \bar{r} \tilde{P}_{12} \frac{\partial \bar{u}_\theta}{\partial \bar{r}} - \tilde{P}_{22} \right], \\ \bar{\rho} \left\{ (\bar{r} + \bar{u}_r) \frac{\partial^2 \bar{u}_\theta}{\partial \bar{t}^2} + 2 \left( \frac{\partial \bar{u}_r}{\partial \bar{t}} \right) \left( \frac{\partial \bar{u}_\theta}{\partial \bar{t}} \right) \right\} &= \frac{1}{\bar{r}} \left[ \frac{\partial}{\partial \bar{r}} (\bar{r} \tilde{P}_{12}) + \bar{r} \tilde{P}_{11} \frac{\partial \bar{u}_\theta}{\partial \bar{r}} - \tilde{P}_{21} \right], \end{aligned} \quad (50)$$

<sup>6</sup>The one-dimensional fine grid solutions were computed with a grid-spacing that was ten times finer than that used for corresponding two-dimensional calculations.

where  $\tilde{P}_{ij}$  are components of a rotated nominal stress tensor defined by

$$\tilde{P} = \bar{R}\bar{P}\bar{R}^T, \quad \bar{R} = \begin{bmatrix} \cos \bar{\theta} & \sin \bar{\theta} \\ -\sin \bar{\theta} & \cos \bar{\theta} \end{bmatrix}, \quad \tilde{R} = \begin{bmatrix} \cos(\bar{\theta} + \bar{u}_\theta) & \sin(\bar{\theta} + \bar{u}_\theta) \\ -\sin(\bar{\theta} + \bar{u}_\theta) & \cos(\bar{\theta} + \bar{u}_\theta) \end{bmatrix}.$$

The components of the rotated stress depend on the displacements as specified by a choice of a constitutive model. For the purposes of this test problem, we consider the SVK model which gives

$$\tilde{P} = \begin{bmatrix} \left(1 + \frac{\partial \bar{u}_r}{\partial \bar{r}}\right) \tilde{S}_{11} & \left(1 + \frac{\bar{u}_r}{\bar{r}}\right) \left(\bar{r} \tilde{S}_{11} \frac{\partial \bar{u}_\theta}{\partial \bar{r}} + \tilde{S}_{12}\right) \\ \left(1 + \frac{\partial \bar{u}_r}{\partial \bar{r}}\right) \tilde{S}_{21} & \left(1 + \frac{\bar{u}_r}{\bar{r}}\right) \left(\bar{r} \tilde{S}_{21} \frac{\partial \bar{u}_\theta}{\partial \bar{r}} + \tilde{S}_{22}\right) \end{bmatrix},$$

where the rotated PK2 stress  $\tilde{S}$  is given as

$$\tilde{S} = \begin{bmatrix} (\bar{\lambda} + 2\bar{\mu})\tilde{E}_{11} + \bar{\lambda}\tilde{E}_{22} & 2\bar{\mu}\tilde{E}_{12} \\ 2\bar{\mu}\tilde{E}_{21} & \bar{\lambda}\tilde{E}_{11} + (\bar{\lambda} + 2\bar{\mu})\tilde{E}_{22} \end{bmatrix},$$

and the rotated Green strain tensor  $\tilde{E}$  is given as

$$\tilde{E} = \frac{1}{2} \begin{bmatrix} \left(1 + \frac{\partial \bar{u}_r}{\partial \bar{r}}\right)^2 + \left(1 + \frac{\bar{u}_r}{\bar{r}}\right)^2 \left(\bar{r} \frac{\partial \bar{u}_\theta}{\partial \bar{r}}\right)^2 - 1 & \left(1 + \frac{\bar{u}_r}{\bar{r}}\right)^2 \left(\bar{r} \frac{\partial \bar{u}_\theta}{\partial \bar{r}}\right) \\ \left(1 + \frac{\bar{u}_r}{\bar{r}}\right)^2 \left(\bar{r} \frac{\partial \bar{u}_\theta}{\partial \bar{r}}\right) & \left(1 + \frac{\bar{u}_r}{\bar{r}}\right)^2 - 1 \end{bmatrix}.$$

The reduced equations in (48) governing the fluid are solved for  $a(t) < r < b$  and  $t > 0$ , where  $a(t) = 1 + \bar{u}_r(1, t)$  is the radial position of the fluid-solid interface. The equations in (50) for the solid are solved in the reference space for  $0 < \bar{r} < 1$  and  $t > 0$ . At the fluid-solid interface, the matching conditions in (12) reduce to

$$v_r = \frac{\partial \bar{u}_r}{\partial t}, \quad -(p - p_e) = \eta \tilde{P}_{11}, \quad 0 = \tilde{P}_{12}, \quad r = a(t), \quad \bar{r} = 1, \quad t > 0,$$

where  $p_e$  is a specified equilibrium pressure and  $\eta = 1/a(t)$ . For the fluid, we take  $\rho = \rho_0$ ,  $v_r = 0$  and  $p = p_e$  at  $t = 0$ , where  $\rho_0$  is a given initial density, and we assume that the outer boundary is a rigid circular wall so that  $v_r = 0$  at  $r = b$ . The initial conditions for the solid are taken to be

$$\bar{u}_r = \bar{u}_\theta = 0, \quad \frac{\partial \bar{u}_r}{\partial t} = \bar{V}(\bar{r}), \quad \frac{\partial \bar{u}_\theta}{\partial t} = 0,$$

where  $\bar{V}(\bar{r})$  is a given initial radial velocity.

The coupled system of differential equations for the fluid and solid, along with the initial conditions, boundary conditions and interface conditions, can be integrated numerically to a final time,  $t_{\text{final}}$ , using a very fine one-dimensional grid in the radial coordinates for the fluid and solid. The one-dimensional solution of the reduced equations describes the solution in the full two-dimensional geometry, and this solution is compared with numerical solutions of the two-dimensional equations obtained using the AMP algorithm without assuming circular symmetry. By analyzing the difference between these solutions, we are able to verify the accuracy and stability of the AMP algorithm for this model FSI problem.

The composite grid used for the rotating disk problem is illustrated in Figure 9. Let  $\mathcal{G}_{\text{rd}}^{(j)}$  denote the grid with resolution factor  $j$  which has grid spacing  $h_j$  approximately equal to  $1/(10j)$ . The two overlapping component grids for the outer fluid domain consist of a Cartesian grid for the square  $[-2, 2] \times [-2, 2]$  together with an annular grid of inner radius  $r_{\text{in}} = a(0) = 1$  and outer radius  $r_{\text{out}} = 1.25$ . The annular grid cuts a hole in the Cartesian grid to form the domain of the fluid. The two overlapping component grids for the inner solid domain consist of a Cartesian grid for the square  $[-1, 1] \times [-1, 1]$  and an annular grid of inner radius  $\bar{r}_{\text{in}} = 0.75$  and outer radius  $\bar{r}_{\text{out}} = r_{\text{in}} = 1$ . The annular grid of the solid trims the outer boundary of the Cartesian grid to form the domain of the solid. The annular grid in the fluid domain deforms at

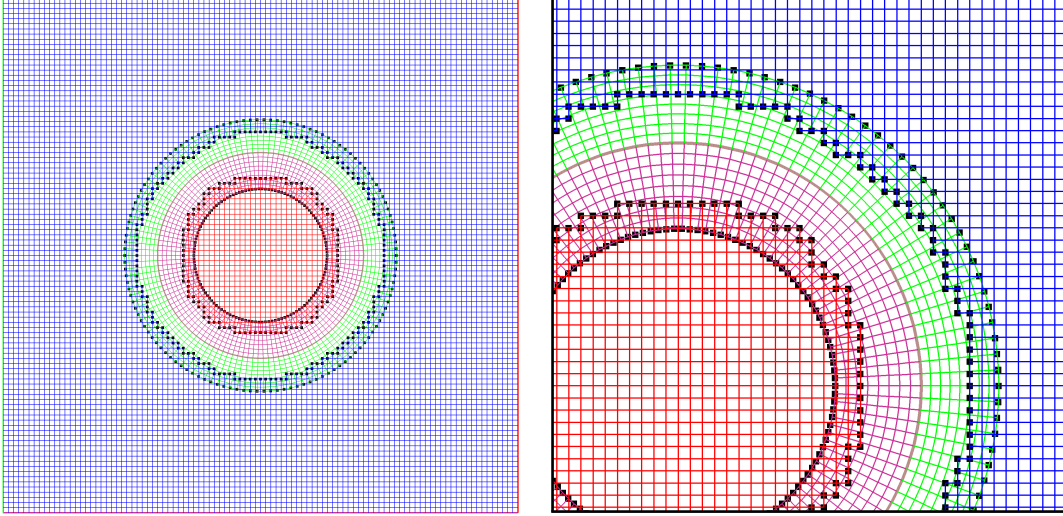


Figure 9: Composite grid  $\mathcal{G}_{\text{rd}}^{(2)}$  for the rotating disk at the initial time. The green annular grid on the fluid side of the interface deforms over time. All other grids remain static.

each time step according to the displacement of the solid at the fluid-solid interface. This interface-fitted grid is generated with the hyperbolic grid generator [37], which uses a marching algorithm starting from the fluid-solid interface to construct the grid.

For the numerical results, we use  $\bar{\rho} = \bar{\lambda} = \bar{\mu} = 1$  for the solid and  $\gamma = 1.4$  for the fluid. The initial density and pressure in the fluid are assumed to be  $\rho_0 = \gamma/\delta$  and  $p_e = 1/\delta$ , respectively, where  $\delta$  is a density ratio parameter. We consider the cases of  $\delta = 0.1$ ,  $\delta = 1$  and  $\delta = 10$ , and refer to these as the *light*, *medium* and *heavy* solid cases, respectively, even though the initial solid density is held fixed and the initial fluid density varies in these three cases. The FSI problem is driven by the initial radial velocity of the solid, which is taken to be

$$\bar{V}(\bar{r}) = \omega_0 [4\bar{r}(1 - \bar{r})]^4,$$

where  $\omega_0 = 0.1$  is a rotation rate parameter. We note that  $\bar{V}(\bar{r})$  approaches zero rapidly enough as  $\bar{r}$  approaches unity to ensure that the corresponding initial motion of the fluid-solid interface is sufficiently smooth in time so that the second-order accuracy of the scheme can be confirmed. The boundary conditions on the fluid at the outer boundary are taken as outflow conditions although this choice is not important since we stop the simulations before the leading outward-traveling disturbance in the fluid reaches the outer boundary.

Figure 10 shows shaded contours of the solution for the case of a light solid with density ratio  $\delta = 0.1$ . These contour plots are obtained from the full two-dimensional solution using  $\mathcal{G}_{\text{rd}}^{(4)}$  and the simplified interface projection. The displacement of the solid is used to plot the solution for the solid in physical space. The plots on the top row show shaded contours of the horizontal components of the velocity in the fluid and the solid at times  $t = 0.5$  and  $t = 1.0$ . The bottom row gives plots of the fluid pressure  $p$  and the solid stress-norm  $|\bar{P}|$  defined as the Frobenius norm of the nominal stress  $\bar{P}$ . The initial radial velocity in the solid generates oscillatory disturbances in the radial and angular displacements. This oscillatory motion in the solid leads to a radially expanding and contracting fluid-solid interface which in turn generates acoustic waves in the fluid that radiate outward from the interface. The radially symmetric elastic waves in the solid and outward-traveling acoustic waves in the fluid are seen in the shaded contour plots at the two times shown.

The line plots in Figure 11 show the behavior of the horizontal component of velocity and stress along  $x_2 = 0$  for density ratios of  $\delta = 0.1$ , 1 and 10. These line plots are taken from two-dimensional solutions using  $\mathcal{G}_{\text{rd}}^{(8)}$  and the simplified interface projection. The plots in the left column show the horizontal velocity in the solid (red) and fluid (blue). We note that the horizontal components of solid and fluid velocities match at the interface along  $x_2 = 0$  in agreement with the interface condition,  $\mathbf{n}^T \mathbf{v} = \mathbf{n}^T \bar{\mathbf{v}}$ , in (12). The difference between the horizontal velocity from the full two-dimensional solution and that determined by the solution

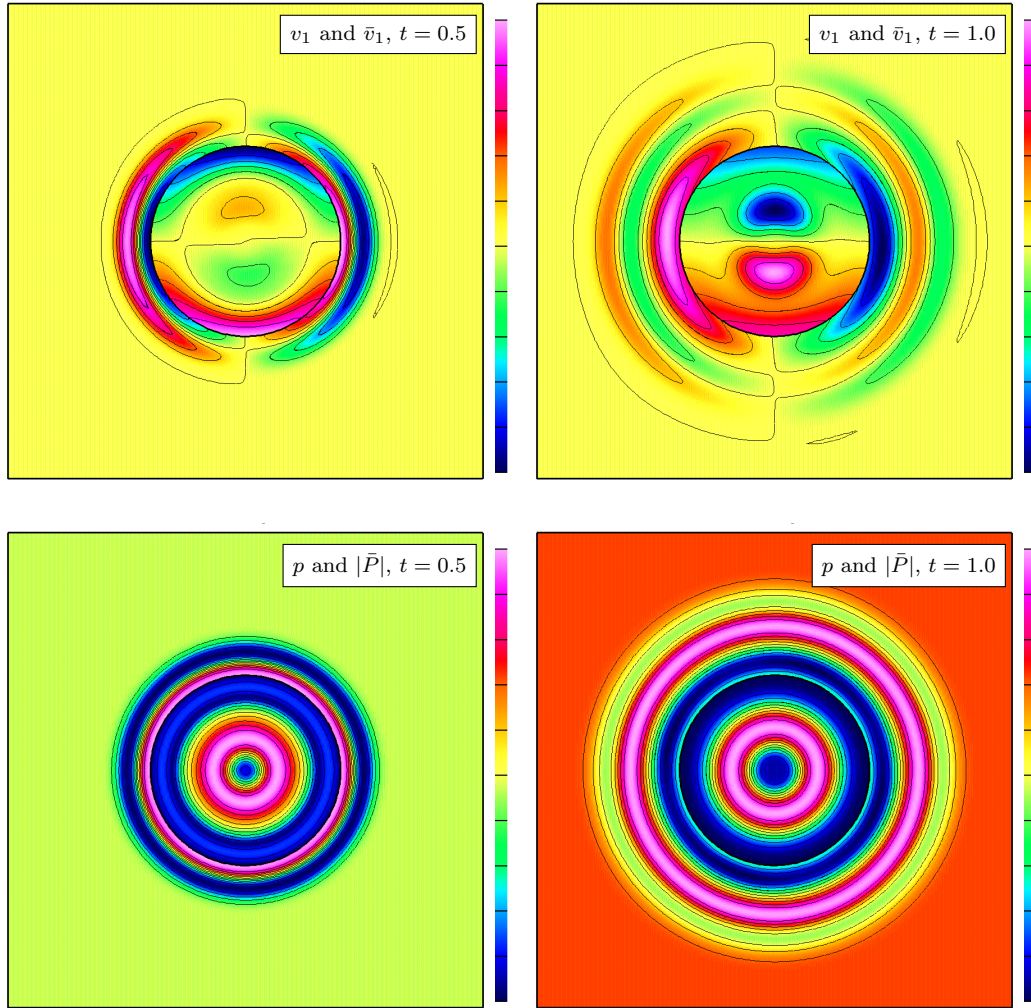


Figure 10: Rotating disk solution contours at times  $t = 0.5$  and  $t = 1.0$  for a light solid  $\delta = 0.1$ , computed on grid  $\mathcal{G}_{\text{rd}}^{(4)}$ . Top: fluid and solid horizontal velocities,  $v_1$  and  $\bar{v}_1$ . Bottom: fluid pressure,  $p$  and solid stress norm  $|\bar{P}|$ . Plot bounds at  $t = 0.5$ :  $v_1 \in [-4.9404 - 05, 4.9440e - 05]$ ,  $\bar{v}_1 \in [-4.99646e - 02, 4.99655e - 02]$ ,  $p \in [9.99934, 10.00073]$ ,  $|\bar{P}| \in [1.7e-04, 4.2e-02]$ , Plot bounds at  $t = 1.0$ :  $v_1 \in [-7.1114e-05, 7.1121e-05]$ ,  $\bar{v}_1 \in [-3.38356698e-02, 3.383561242e-02]$ ,  $p \in [9.999058, 10.00037]$ ,  $|\bar{P}| \in [5.35 - 04, 5.42e - 02]$ .

of the reduced one-dimensional equations is shown by the black curves in the velocity plots. The amplitude of these curves is small indicating excellent agreement between the two solutions. (The behavior of the error is described in more detail in the tables below.) The behavior of the horizontal component of the Cauchy stress in the solid, given by  $\bar{\sigma}_{11}$  in blue, and the adjusted fluid pressure, given by  $p_e - p$  in red, is shown in the plots in the right column of the figure. As in the plots of the velocity, we see that the stresses also match at the interface along  $x_2 = 0$  in agreement with the interface condition in (12) involving stress.

The tables in Figures 12, 13 and 14 give maximum errors and estimated convergence rates for numerical solutions of the rotating disk problem at  $t = 0.5$  for the density ratios  $\delta = 10$ , 1 and  $10^{-1}$ , respectively. Results for the AMP algorithm using the simplified projection are compared to those using the full projection. The two sets of results are nearly identical and both show the expected second-order accuracy for all three cases. The case of the light solid is the most difficult case as the FSI problem is approaching that of inviscid fluid with a free surface; note that the ratios are getting closer to 4 as the grid is refined. In general, we have found that the difference between solutions computed using the simplified projection and the full projection is negligible for the FSI problems considered in this paper. For the heavy solid case, we also present errors and convergence rates for solutions obtained using a traditional partitioned (TP) scheme in which the velocity of the solid provides a boundary condition on the fluid and the traction from the fluid gives a forcing on the

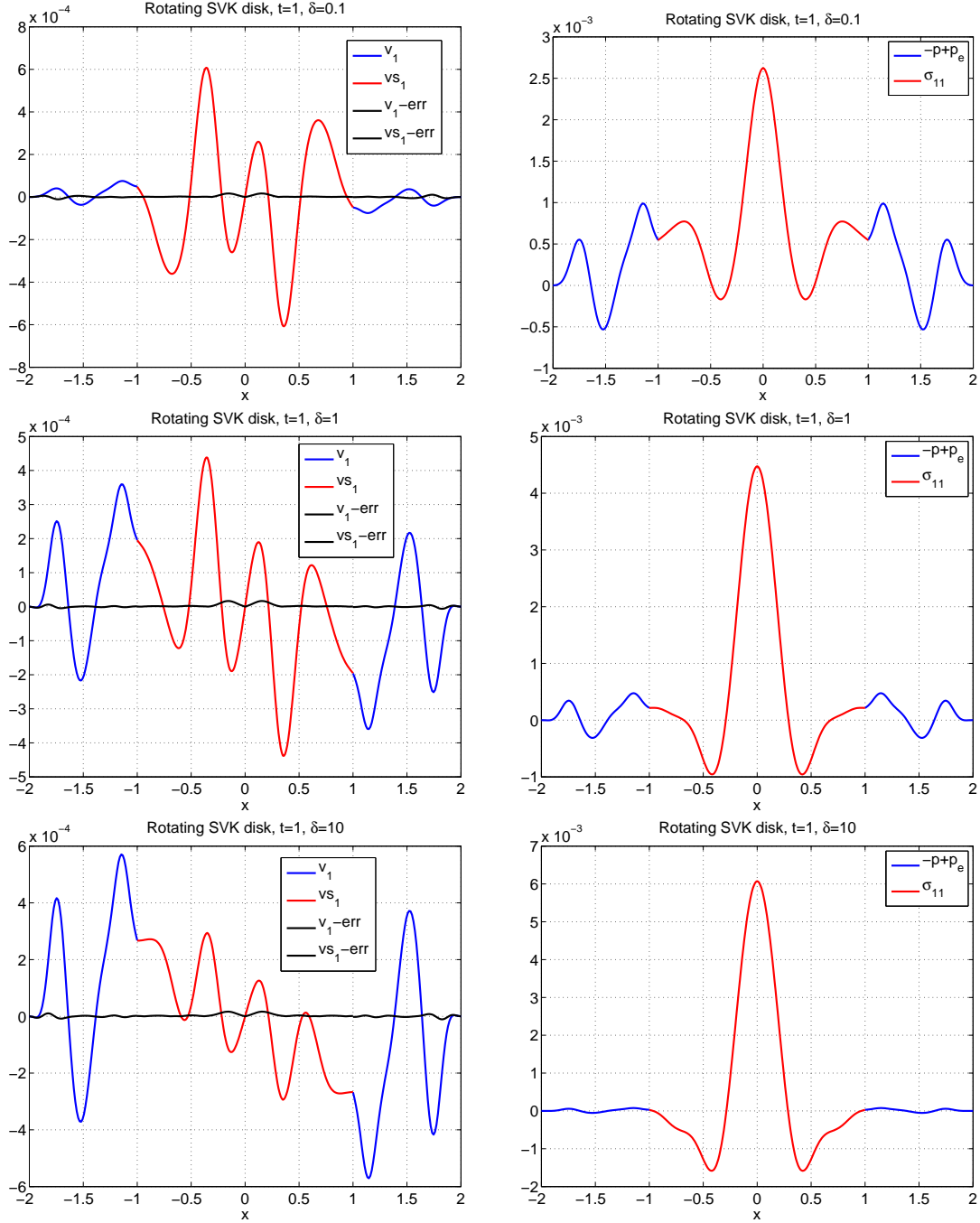


Figure 11: Rotating disk line plots. Solution components plotted along the line  $y = 0$  at  $t = 1$  using grid  $\mathcal{G}_{rd}^{(8)}$ . Top: light-solid,  $\delta = 0.1$ . Middle: medium solid,  $\delta = 1$ . Bottom: heavy solid,  $\delta = 10$ .

solid (i.e. the traditional Dirichlet-Neumann coupling, see [1, 4]). The results for the TP scheme are very close to those of the present AMP algorithm for  $\delta = 10$ , but the TP scheme was found to be unstable for the medium ( $\delta = 1$ ) and light ( $\delta = 0.1$ ) solid cases.

## 6. Interaction of a planar shock and an elliptical solid

In this section, we study the interaction of a planar shock in a fluid with a solid that is initially in the shape of an ellipse and is oblique to the incoming shock. Solutions of this FSI problem are computed

Rotating disk, heavy solid, simplified projection, $\delta = 10$														
$h_j$	$E_j^{(\rho)}$	$r$	$E_j^{(v_1)}$	$r$	$E_j^{(v_2)}$	$r$	$E_j^{(T)}$	$r$	$E_j^{(\bar{u})}$	$r$	$E_j^{(\bar{v})}$	$r$	$E_j^{(\bar{P})}$	$r$
1/20	1.5e-5		1.1e-4		1.1e-4		3.1e-5		1.7e-4		1.0e-3		1.5e-3	
1/40	4.1e-6	3.7	2.9e-5	3.7	3.0e-5	3.5	8.3e-6	3.7	2.9e-5	5.7	2.3e-4	4.5	2.1e-4	6.9
1/80	9.6e-7	4.3	6.6e-6	4.4	6.7e-6	4.5	1.9e-6	4.3	5.6e-6	5.3	4.8e-5	4.8	3.9e-5	5.4
1/160	2.4e-7	4.1	1.6e-6	4.1	1.6e-6	4.1	4.8e-7	4.1	1.2e-6	4.8	1.1e-5	4.5	8.3e-6	4.8
rate	2.01		2.02		2.03		2.01		2.39		2.20		2.48	

Rotating disk, heavy solid, full projection, $\delta = 10$														
$h_j$	$E_j^{(\rho)}$	$r$	$E_j^{(v_1)}$	$r$	$E_j^{(v_2)}$	$r$	$E_j^{(T)}$	$r$	$E_j^{(\bar{u})}$	$r$	$E_j^{(\bar{v})}$	$r$	$E_j^{(\bar{P})}$	$r$
1/20	1.5e-5		1.1e-4		1.1e-4		3.1e-5		1.7e-4		1.0e-3		1.5e-3	
1/40	4.1e-6	3.7	2.9e-5	3.7	3.0e-5	3.5	8.3e-6	3.7	2.9e-5	5.7	2.3e-4	4.5	2.1e-4	6.9
1/80	9.6e-7	4.3	6.6e-6	4.4	6.7e-6	4.5	1.9e-6	4.3	5.6e-6	5.3	4.8e-5	4.8	3.9e-5	5.4
1/160	2.4e-7	4.1	1.6e-6	4.1	1.6e-6	4.1	4.8e-7	4.1	1.2e-6	4.8	1.1e-5	4.5	8.3e-6	4.8
rate	2.01		2.02		2.03		2.01		2.39		2.20		2.48	

Rotating disk, heavy solid, traditional partitioned, $\delta = 10$														
$h_j$	$E_j^{(\rho)}$	$r$	$E_j^{(v_1)}$	$r$	$E_j^{(v_2)}$	$r$	$E_j^{(T)}$	$r$	$E_j^{(\bar{u})}$	$r$	$E_j^{(\bar{v})}$	$r$	$E_j^{(\bar{P})}$	$r$
1/20	1.4e-5		1.0e-4		1.0e-4		2.9e-5		1.7e-4		1.0e-3		1.4e-3	
1/40	3.9e-6	3.8	2.8e-5	3.7	2.9e-5	3.5	7.9e-6	3.7	2.9e-5	5.7	2.3e-4	4.4	2.1e-4	6.9
1/80	9.4e-7	4.1	6.5e-6	4.2	6.6e-6	4.4	1.9e-6	4.1	5.6e-6	5.3	4.8e-5	4.8	3.9e-5	5.4
1/160	2.3e-7	4.1	1.6e-6	4.1	1.6e-6	4.1	4.7e-7	4.1	1.2e-6	4.7	1.1e-5	4.5	8.2e-6	4.7
rate	2.00		2.00		2.01		2.00		2.38		2.19		2.48	

Figure 12: Rotating SVK disk, heavy solid. Maximum errors and estimated convergence rates at  $t = 0.5$ , computed using the AMP scheme for a heavy solid,  $\delta = 10$ . Results are shown for the simplified projection, full projection and traditional partitioned scheme.

Rotating disk, medium solid, simplified projection, $\delta = 1$														
$h_j$	$E_j^{(\rho)}$	$r$	$E_j^{(v_1)}$	$r$	$E_j^{(v_2)}$	$r$	$E_j^{(T)}$	$r$	$E_j^{(\bar{u})}$	$r$	$E_j^{(\bar{v})}$	$r$	$E_j^{(\bar{P})}$	$r$
1/20	1.1e-4		7.3e-5		7.5e-5		2.1e-5		1.7e-4		1.0e-3		1.5e-3	
1/40	3.2e-5	3.3	2.3e-5	3.2	2.3e-5	3.2	6.6e-6	3.2	2.9e-5	5.7	2.3e-4	4.5	2.1e-4	6.9
1/80	8.3e-6	3.9	5.8e-6	4.0	5.8e-6	4.0	1.7e-6	3.9	5.6e-6	5.3	4.8e-5	4.8	3.9e-5	5.5
1/160	2.1e-6	4.0	1.5e-6	4.0	1.5e-6	4.0	4.3e-7	4.0	1.2e-6	4.8	1.1e-5	4.5	8.1e-6	4.8
rate	1.89		1.89		1.90		1.89		2.39		2.20		2.49	

Rotating disk, medium solid, full projection, $\delta = 1$														
$h_j$	$E_j^{(\rho)}$	$r$	$E_j^{(v_1)}$	$r$	$E_j^{(v_2)}$	$r$	$E_j^{(T)}$	$r$	$E_j^{(\bar{u})}$	$r$	$E_j^{(\bar{v})}$	$r$	$E_j^{(\bar{P})}$	$r$
1/20	1.1e-4		7.3e-5		7.5e-5		2.1e-5		1.7e-4		1.0e-3		1.5e-3	
1/40	3.2e-5	3.3	2.3e-5	3.2	2.3e-5	3.2	6.6e-6	3.2	2.9e-5	5.7	2.3e-4	4.5	2.1e-4	6.9
1/80	8.3e-6	3.9	5.8e-6	4.0	5.8e-6	4.0	1.7e-6	3.9	5.6e-6	5.3	4.8e-5	4.8	3.9e-5	5.5
1/160	2.1e-6	4.0	1.5e-6	4.0	1.5e-6	4.0	4.3e-7	4.0	1.2e-6	4.8	1.1e-5	4.5	8.1e-6	4.8
rate	1.89		1.89		1.90		1.89		2.39		2.20		2.49	

Figure 13: Rotating SVK disk, medium solid. Maximum errors and estimated convergence rates at  $t = 0.5$ , computed using the AMP scheme medium solid,  $\delta = 1$ . Results are shown for the simplified and full projections, the traditional partitioned scheme is unstable in this case.

assuming the fluid is an ideal gas, and for two different hyperelastic constitutive models for the solid, namely, the neo-Hookean (NH) constitutive law in (10) and linearly-elastic (LE) constitutive law in (11). The ratio of the density of the solid to that in the fluid is taken to be small so that added-mass effects are significant. The numerical solutions of the FSI problem are computed using the AMP algorithm with the simplified AMP projection given in (29) for both of these cases. The intent of this study is to demonstrate the stability and accuracy of the AMP algorithm for a complex light-solid FSI problem, and also to contrast the behavior of solutions obtained using two different solid models for a FSI problem exhibiting a large solid rotation. For this latter comparison, we also find it helpful to consider the numerical solution of the FSI problem assuming the solid is rigid. The solution of the rigid-body (RB) case is computed using the approach for light rigid

Rotating disk, light solid, simplified projection, $\delta = 0.1$														
$h_j$	$E_j^{(\rho)}$	$r$	$E_j^{(v_1)}$	$r$	$E_j^{(v_2)}$	$r$	$E_j^{(T)}$	$r$	$E_j^{(\bar{u})}$	$r$	$E_j^{(\bar{v})}$	$r$	$E_j^{(P)}$	$r$
1/20	1.1e-3		4.0e-5		2.7e-5		5.7e-5		1.8e-4		1.2e-3		1.5e-3	
1/40	1.8e-4	5.9	1.3e-5	3.1	1.3e-5	2.1	3.8e-6	15.2	3.2e-5	5.6	2.9e-4	4.2	2.2e-4	6.8
1/80	6.3e-5	2.9	4.4e-6	2.9	4.4e-6	2.9	1.3e-6	2.9	6.2e-6	5.2	6.4e-5	4.5	4.2e-5	5.2
1/160	1.8e-5	3.6	1.3e-6	3.5	1.2e-6	3.6	3.6e-7	3.6	1.3e-6	4.7	1.5e-5	4.4	9.2e-6	4.6
rate	1.94		1.65		1.49		2.35		2.36		2.13		2.45	

Rotating disk, light solid, full projection, $\delta = 0.1$														
$h_j$	$E_j^{(\rho)}$	$r$	$E_j^{(v_1)}$	$r$	$E_j^{(v_2)}$	$r$	$E_j^{(T)}$	$r$	$E_j^{(\bar{u})}$	$r$	$E_j^{(\bar{v})}$	$r$	$E_j^{(P)}$	$r$
1/20	1.1e-3		4.0e-5		2.7e-5		5.7e-5		1.8e-4		1.2e-3		1.5e-3	
1/40	1.8e-4	5.9	1.3e-5	3.1	1.3e-5	2.1	3.8e-6	15.3	3.2e-5	5.6	2.9e-4	4.2	2.2e-4	6.8
1/80	6.3e-5	2.9	4.4e-6	2.9	4.4e-6	2.9	1.3e-6	2.9	6.2e-6	5.2	6.4e-5	4.5	4.2e-5	5.2
1/160	1.8e-5	3.6	1.3e-6	3.5	1.2e-6	3.6	3.6e-7	3.6	1.3e-6	4.7	1.5e-5	4.4	9.2e-6	4.6
rate	1.94		1.65		1.49		2.35		2.36		2.13		2.45	

Figure 14: Rotating SVK disk, light solid. Maximum errors and estimated convergence rates at  $t = 0.5$ , computed using the AMP scheme medium solid,  $\delta = 0.1$ . Results are shown for the simplified and full projections, the traditional partitioned scheme is unstable in this case.

bodies described in [2]. We also compare numerical solution for the NH case using the full AMP projection given in (28) with that obtained using the simplified projection.

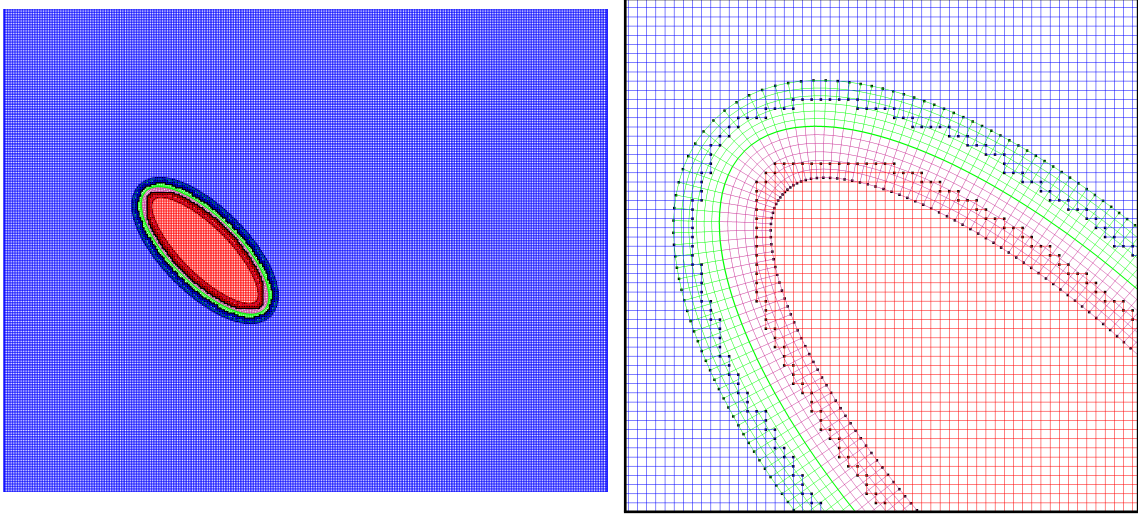


Figure 15: Composite grid  $\mathcal{G}_e^{(4)}$  for the fluid surrounding a deforming elliptical solid at  $t = 0$ . The solid domain is discretized with the red Cartesian grid and the pink boundary-fitted hyperbolic grid. The fluid domain is discretized with the blue Cartesian grid and the green hyperbolic grid fitted to the elliptical boundary of the solid. The green grid deforms over time while all other grids remain static.

At the initial time,  $t = 0$ , the center of the elliptical solid is located at  $\mathbf{x} = (-1, 0)$  and its major axis is tilted 45 degrees with respect to the planar shock initially located at  $\mathbf{x} = (-2.25, 0)$  and traveling in the positive  $x_1$ -direction. The lengths of the semi-axes of the ellipse are 1.25 and 0.5. The density of the solid is taken to be  $\bar{\rho} = 0.1$ , and for the elastic NH and LE cases the solid material parameters are chosen to be  $\bar{\lambda} = \bar{\mu} = 4$ . The ratio of specific heats for the gas is assumed to be  $\gamma = 1.4$ , and the initial shock Mach number is taken to be  $M = 1.3$ . The ambient state of the gas ahead of the shock in primitive variables is  $[\rho, v_1, v_2, p] = [1, 0, 0, 1]$ , and the corresponding state behind the shock is  $[1.516, 0.5233, 0, 1.191]$  as determined by the usual shock jump conditions [43].

The composite grid for the deforming ellipse geometry is denoted by  $\mathcal{G}_e^{(j)}$  and has grid spacing  $h_j \approx 1/(10j)$  for the grid resolution factor  $j$ . The composite grid consists of four component grids as illustrated

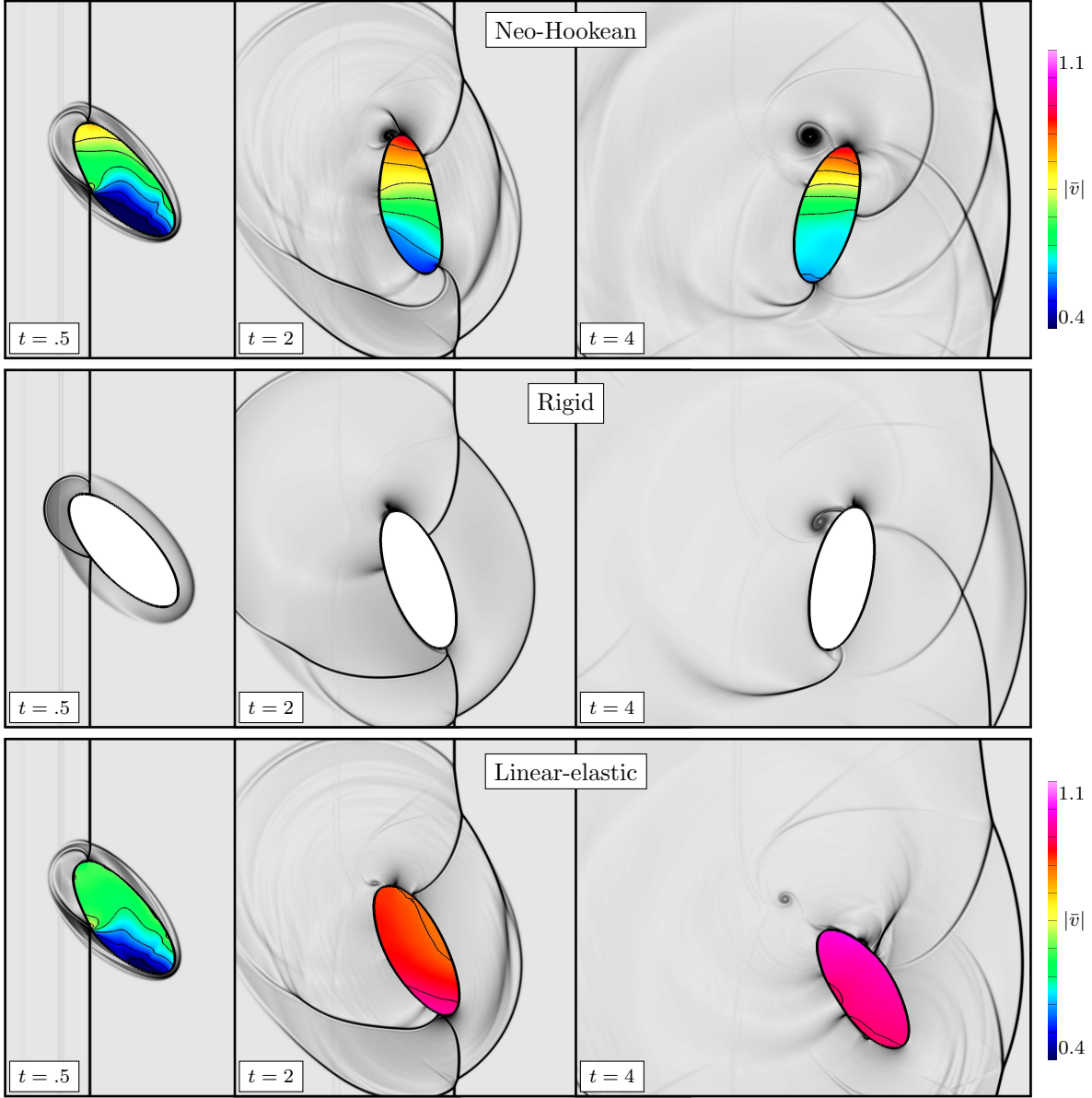


Figure 16: Planar shock impacting an elliptical solid. A comparison of the solutions obtained using the Neo-Hookean model (top), rigid body model (middle), and linearly-elasticity model (bottom) at times  $t = 0.5$  (left),  $t = 2.0$  (middle) and  $t = 4.0$  (right).

in Figure 15 for the case  $j = 4$  at  $t = 0$ . The elliptical solid domain in the reference space is represented by a static rectangular grid  $\mathcal{R}_s$  for the domain  $[-2.75, .75] \times [1.75, 1.75]$  and an overlapping static boundary-fitted grid generated by the hyperbolic grid generator from the fluid-solid interface represented by a spline. The fluid domain in the physical space is also represented by two component grids: a static background rectangular grid  $\mathcal{R}_f$  on the domain  $[-4, 5] \times [-4, 4]$  and an overlapping boundary-fitted grid that moves according to the computed deformation of the fluid-solid interface. The latter grid is generated from the fluid-solid interface in physical space using the hyperbolic grid generator. Both hyperbolic grids have 6 grid lines in the normal direction (plus ghost lines). To give an indication of the number of grid points involved, the finest composite grid used for the simulations presented in this section is  $\mathcal{G}_e^{(16)}$  which has approximately

2.2 million grid points. We note, however, that only about 8,800 of these grid points belong to the two curvilinear component grids so that a large percentage of the total grid points lie on Cartesian grids. The fluid and solid domain solvers are optimized for Cartesian grids and thus the total cost of the simulations is dominated by the cost of advancing the numerical solution on static Cartesian grids with a relatively small portion of the total cost needed to handle grid motion and deformation.

Figure 16 shows the solutions at times  $t = 0.5, 2.0$  and  $4.0$  for the NH, RB and LE solid models in rows from top to bottom. The solution in the fluid domain is illustrated using numerical schlieren images which describe the behavior of the gradient of density (see [8] for the definition). This choice highlights the complex wave behavior (shocks and contacts) in the fluid. Shaded contours of the magnitude of the solid velocity,  $|\bar{\mathbf{v}}| = \sqrt{\bar{v}_1^2 + \bar{v}_2^2}$ , are shown in the (deforming) solid domains. The solutions at time  $t = 0.5$  depict the state shortly after the shock has impacted the solid. At this time the NH and LE results are similar with the leading (left-hand) region of the solid clearly being deformed by the shock. For the RB case, the entire rigid body accelerates immediately upon impact with the incident planar shock, which then generates a bow shock in the fluid seen to the right of the body. Similar bow shocks are observed in the NH and LE cases, but their generation is delayed by the time required for the elastic waves to traverse the solid. By the intermediate time  $t = 2$  there are clear differences between the results from the three solid models, and these differences become larger at the later time  $t = 4$ . The LE model, which assumes that  $\|\bar{\mathbf{u}}_{\mathbf{x}}\| = \|\bar{\mathbf{F}} - \mathbf{I}\| \ll 1$ , is not suitable for FSI problem with large solid rotations and this property is clearly evident: the LE solid does not rotate very much but rather moves on a trajectory downward and to the right. The overall motion of the solid for the NH and RB models is similar, although the solid for the RB model has moved somewhat further to the right. Another feature that appears in the fluid schlieren images is that, compared to the results for the rigid body, the NH and LE results show many low amplitude waves in the fluid that are generated by the elastic waves in the solid interacting with the interface after the impact with the shock.

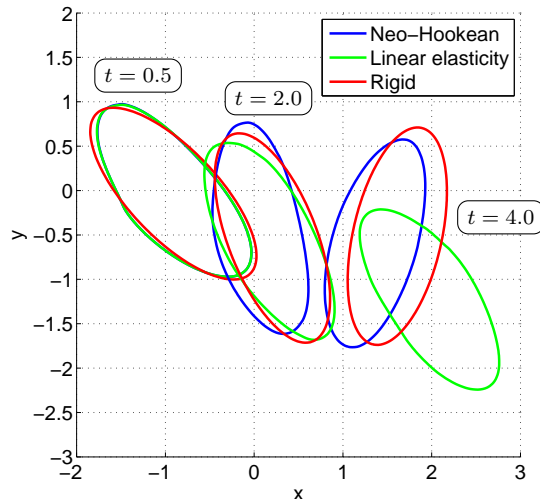


Figure 17: Planar shock impacting an elliptical solid. A comparison of the evolution of the solid boundary for the Neo-Hookean model (blue), rigid body model (red), and linearly-elasticity model (green) at  $t = 0.5, 2.0$  and  $4.0$ .

Figure 17 shows the behavior of the solid boundary from the solutions described in Figure 16 on the same graph. At the early time,  $t = 0.5$ , the positions of the solid boundaries determined by the NH model (blue) and LE model (green) are very close. At this time, the deformation is relatively small so that the deformation gradient tensor is close the identity and the LE model is a good approximation of the NH model. The boundary given by the RB solution shows some difference in comparison to the other two solutions. At the two later times, the solid boundary given by the LE solution continues to translate but with little rotation in agreement with the solutions shown in Figure 16. In contrast, the boundaries given by solutions of the NH and RB models shown translation and significant rotation, and with some differences in the position of the solid boundaries as expected.

The convergence of the numerical solution can be judged by comparing solutions obtained using composite

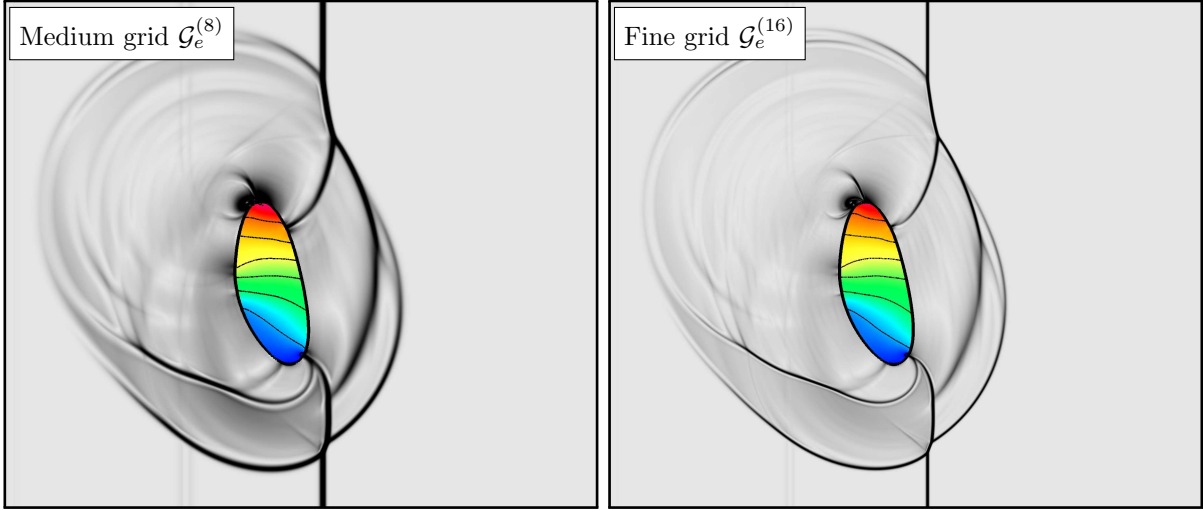


Figure 18: Planar shock impacting an elliptical solid. A comparison of solutions for the medium resolution grid  $\mathcal{G}_e^{(8)}$  (left) and the fine grid  $\mathcal{G}_e^{(16)}$  (right) for the neo-Hookean solid model at  $t = 2.0$ .

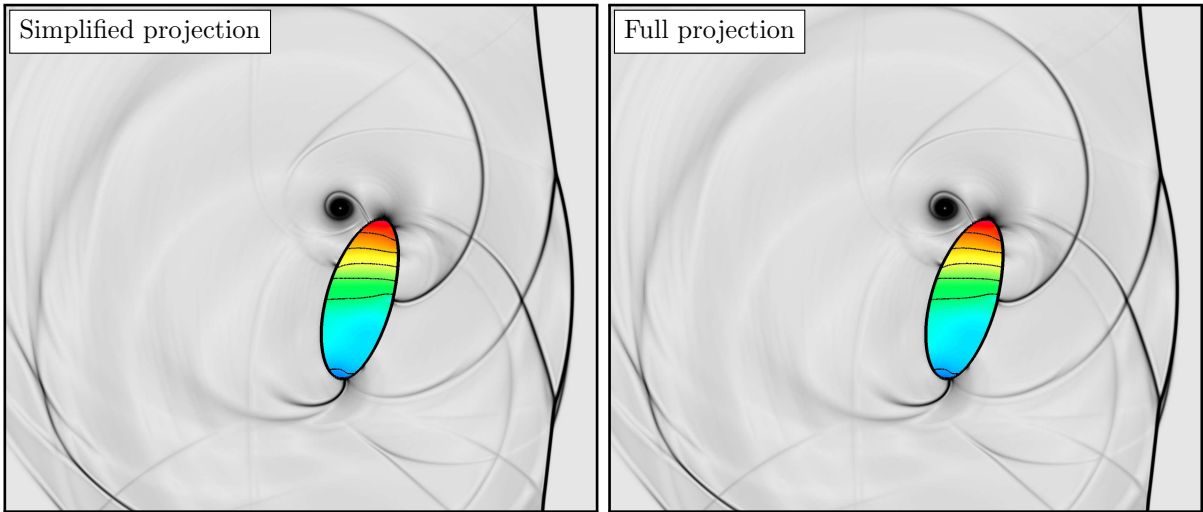


Figure 19: Planar shock impacting an elliptical solid. A comparison of solutions using the simplified AMP projection (left) and the full AMP projection (right) for the neo-Hookean solid model with grid  $\mathcal{G}_e^{(16)}$  at  $t = 4.0$ .

grids with different resolutions. Figure 18 shows numerical solutions of the FSI problem for the NH solid model at  $t = 2.0$  using the grids  $\mathcal{G}_e^{(8)}$ , medium resolution (left), and  $\mathcal{G}_e^{(16)}$ , fine resolution (right). Differences in the two solutions are observed in the thickness of shocks and contacts in the fluid, as expected, but there is generally very good agreement between the two solutions. The qualitative agreement shown in the figure for the planar shock/elliptical solid FSI problem supports the results of the detailed quantitative convergence studies discussed in the previous section of the paper.

The numerical solutions described here for the NH and LE solids models are computed using the AMP algorithm with the simplified projection formulas in (29). As mentioned earlier, we have found that there is negligible difference between solutions obtained using the simplified projection and those obtained using the full projection formulas in (28) for all FSI problems we have studied. Figure 19 illustrates this observation for solutions of the planar shock/elliptical solid FSI problem for the NH solid model. The figure shows two solutions, one using the simplified projection (left) and the other using the full projection (right). Both

solutions are computed using the composite grid  $\mathcal{G}_e^{(16)}$  and the results are shown at  $t = 4.0$ . We observe no distinguishable difference between the two solutions in agreement with the results of previously discussed FSI problems.

## 7. Flexible solid beam in a cross flow

As a final demonstration of the AMP scheme we consider high speed flow past a thin flexible beam in a fluid channel. This example illustrates the capability of the numerical approach to handle light flexible solids undergoing large deformations. The geometry of the problem at the initial time consists of a vertical solid beam, fixed at its base and parallel to the  $y$ -axis, in a fluid channel of dimensions  $[x_a, x_b] \times [y_a, y_b] = [-1, 2] \times [0, 1.5]$ . The height of the beam is 1.0, while the thickness is approximately 0.1 over its length, except near the rounded free end<sup>7</sup>, as shown in Figure 20.

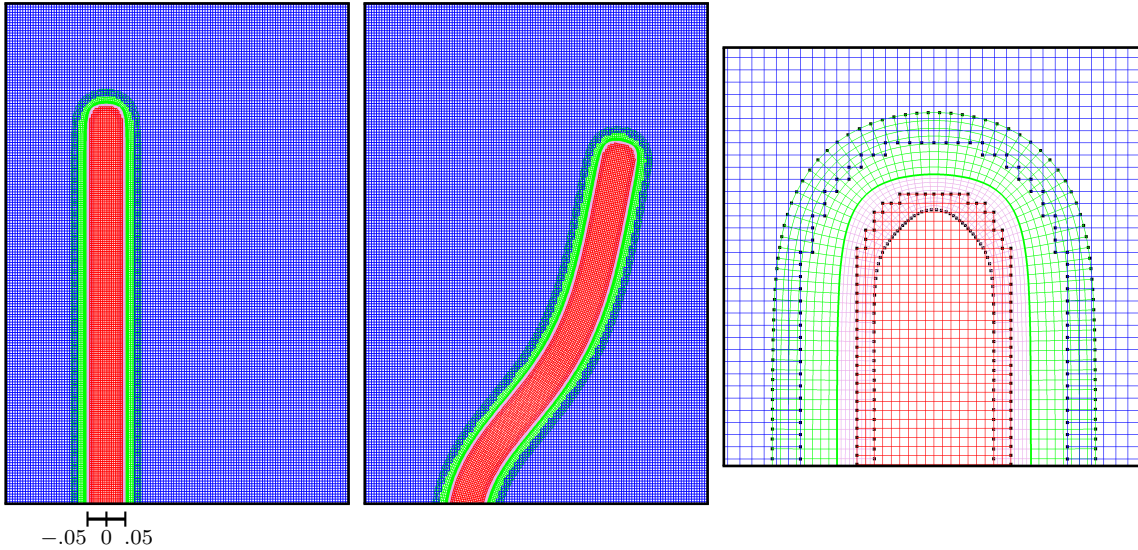


Figure 20: Composite grid  $\mathcal{G}_{bic}^{(16)}$  for a deforming solid beam in a channel at two times and a magnified view near the rounded tip. The solid domain is discretized with the red Cartesian grid and the pink boundary-fitted hyperbolic grid. The fluid domain is discretized with the blue Cartesian grid and the green hyperbolic grid. The green fluid grid deforms over time while all other grids remain static (the solid grids are adjusted by the displacement for plotting purposes).

The composite grid for the beam in a channel geometry is denoted by  $\mathcal{G}_{bic}^{(j)}$  and has grid spacing  $h_j \approx 1/(10j)$  for the grid resolution factor  $j$ . The composite grid consists of four component grids as illustrated in Figure 20 for the case  $j = 16$ . The fluid domain is discretized with a background Cartesian grid together with a hyperbolic grid adjacent to the beam surface. The hyperbolic grid is constructed by marching 9 grid lines in the normal direction. The solid domain is also discretized with a background grid and a hyperbolic grid with 10 grid lines in the normal direction. The average grid spacings in the two solid grids are approximately 1.2 times smaller than those in the fluid grids in order to better resolve the thin solid domain.

The fluid is taken to be an ideal gas with ratio of specific heats  $\gamma = 1.4$ . The solid, modeled by the neo-Hookean constitutive law, is chosen to be quite light and flexible with different material parameters chosen for the four cases considered below. The fluid and solid are initially at rest and in mechanical equilibrium. The initial state of the gas in primitive variables is  $[\rho, v_1, v_2, p] = [1, 0, 0, 1/\gamma] \equiv \mathbf{q}_0$ . The initial displacement, velocity and stress in the solid are zero, and the equilibrium pressure,  $p_e = 1/\gamma$ , is chosen to match the

<sup>7</sup> The boundary of the beam, including its rounded end, is defined in terms of hyperbolic trigonometric functions through the *SmoothedPolygon* mapping [44]. The precise definition of the grid and the scripts to run the simulations presented in this section (and previous sections) are available with the *Overture* software at [overtureFramework.org](http://overtureframework.org).

initial fluid pressure. The flow is smoothly accelerated by specifying the inflow boundary condition as

$$[\rho, v_1, v_2, p] = \mathbf{q}_0 + (\mathbf{q}_1 - \mathbf{q}_0)R(t), \quad \text{for } x = x_a, \quad t > 0, \quad (51)$$

where  $[\rho, v_1, v_2, p] = [1.1691, 0.1591, 0, .8893] \equiv \mathbf{q}_1$  is the inflow state reached for  $t \geq 1$ , and where  $R(t)$  is a smooth *ramp* function given by

$$R(t) = \begin{cases} (3 - 2t)t^2, & \text{for } 0 \leq t \leq 1, \\ 1, & \text{for } t > 1. \end{cases} \quad (52)$$

The ramp function satisfies  $R(0) = 0$ ,  $R(1) = 1$  and  $R'(0) = R'(1) = 0$ . The final state  $\mathbf{q}_1$  was chosen to correspond to the state behind a shock with shock Mach number equal to 1.1. The boundary conditions on the top and bottom of the fluid domain are taken as slip walls, while an outflow boundary condition is specified at  $x = x_b$ . The bottom boundary of the solid at  $y = y_a$  is specified as a zero displacement boundary. The interface between the fluid and solid is treated with the simplified AMP projection scheme.

The images in Figure 21 provide snapshots of the solution at  $t = 1, 2, \dots, 6$  for a solid beam with  $\bar{\rho} = \bar{\lambda} = \bar{\mu} = 10$ . The instantaneous streamlines in the fluid are shown along with shaded contours of the solid speed,  $|\bar{\mathbf{v}}|$ . The fluid flow traveling to the right from the ramped inflow boundary at  $x = x_a$  reaches the beam at  $t \approx 1$ . The maximum horizontal acceleration of the beam occurs along its central portion initially due to the largest fluid stresses there, and this causes the beam to bend concave to the left at early times. Later the top portion of the beam experiences the highest acceleration which causes the beam to bend concave to the right by  $t = 6$ . The beam undergoes large deformations, with correspondingly large displacement of the body-fitted fluid grid, and this FSI problem is computed effectively with the AMP scheme on deforming composite grids.

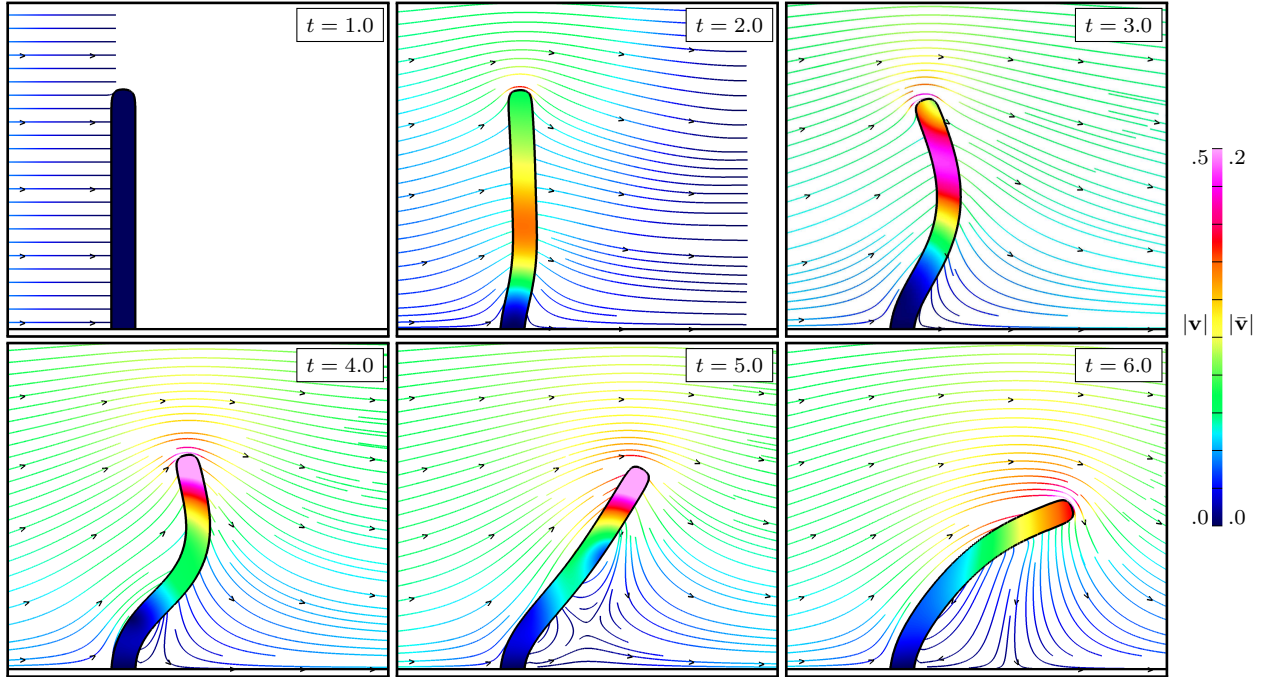


Figure 21: Flow past a solid beam in a channel. Instantaneous streamlines in the fluid and speed of solid at times  $t = 1, 2, \dots, 6$  for  $\bar{\rho} = \bar{\lambda} = \bar{\mu} = 10$ , computed on grid  $\mathcal{G}_{bic}^{(32)}$ .

Figure 22 shows the position of the centerline of beams at various times and for different sets of material parameters. The position  $\mathbf{x}$  of the centerline at a given time  $t$  is defined by  $\mathbf{x} = \bar{\mathbf{x}} + \bar{\mathbf{u}}(\bar{\mathbf{x}}, t)$  along the vertical line segment from  $\bar{\mathbf{x}} = (0, 0)$  to  $(0, 1)$  in the reference domain of the solid. The displacement  $\bar{\mathbf{u}}$  is determined by interpolation of the composite-grid solution for the solid onto this line segment. All beams considered

are light and flexible. The heaviest beam has a density of only 100 times that of the ambient air, while the lightest beam has a density equal to the ambient air. The initial motions of the beams are similar in all cases although the light and more flexible beams undergo larger deformations. Note that the two heavier cases are shown at times  $t = 0, 2, 4, \dots, 14$ , while the two lighter cases are shown at times  $t = 0, 1, 2, 3, \dots, 7$ . The heaviest and stiffest beam considered, with  $\bar{\rho} = 100$  and  $\bar{\lambda} = \bar{\mu} = 100$ , undergoes a fairly large deflection of approximately 40% of its length in the horizontal direction. The very lightest beam considered, with  $\bar{\rho} = 1$  and  $\bar{\lambda} = \bar{\mu} = 10$ , bends over dramatically by  $t = 5$ , and has started to bend back upwards by the final time shown,  $t = 7$ .

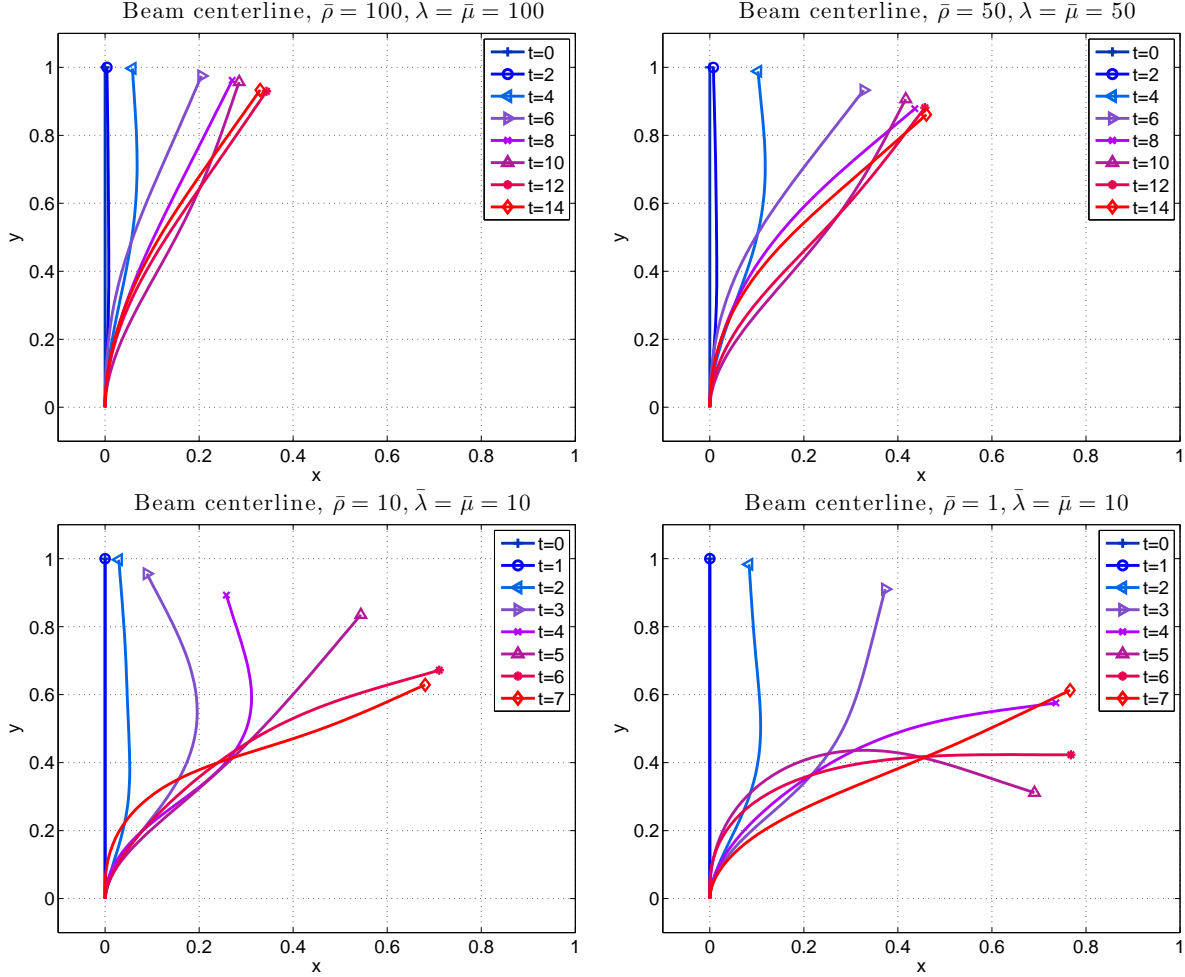


Figure 22: Position of the centerline of beams with different material properties.

Figure 23 shows results from a grid convergence study. The position of the beam centerline is compared at different times for computations using the coarse grid  $\mathcal{G}_{bic}^{(16)}$  and the finer grid  $\mathcal{G}_{bic}^{(32)}$ . Results for two different cases are presented: the heavier and stiffer beam with  $\bar{\rho} = \bar{\lambda} = \bar{\mu} = 100$  is compared at times  $t = 0, 2, 4, \dots, 14$ , while the lighter and more flexible beam with  $\bar{\rho} = \bar{\lambda} = \bar{\mu} = 10$  is compared at times  $t = 0, 1, 2, \dots, 7$ . In both cases the fine and coarse grid results are in excellent agreement. Only slight differences start to appear for later times as would be expected.

## 8. Conclusions

We have developed a new *added mass partitioned* (AMP) algorithm for simulating FSI problems that couple inviscid compressible fluids and nonlinear hyperelastic solids. The AMP algorithm uses a mixed Eulerian-Lagrangian approach on deforming composite grids (DCG) so that large changes in geometry can

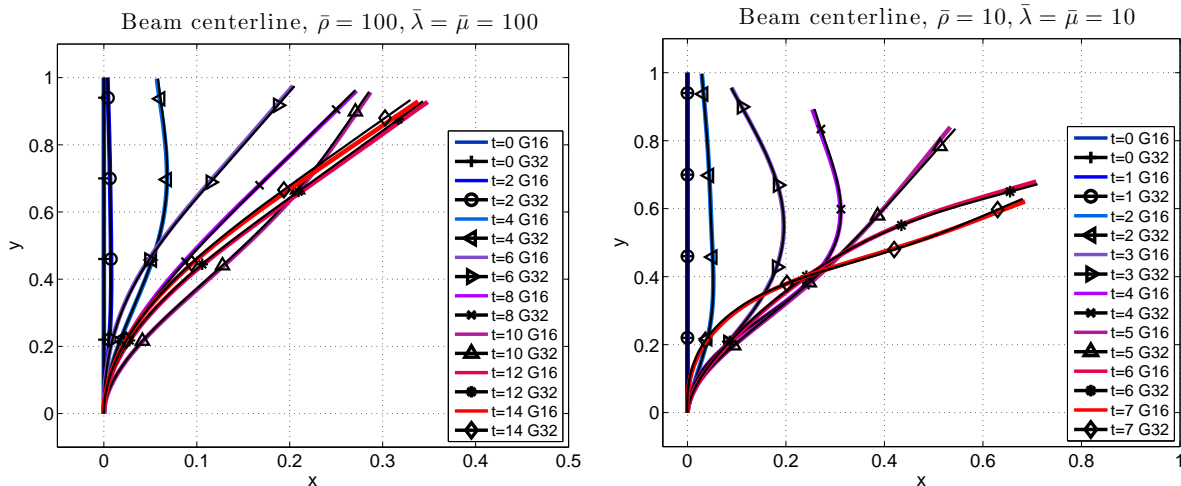


Figure 23: Grid convergence of the beam centerline. Comparison of the solutions from the coarse grid  $\mathcal{G}_{bic}^{(16)}$  (colored lines) and the finer grid  $\mathcal{G}_{bic}^{(32)}$  (black lines with symbols).

be handled efficiently while maintaining high-quality grids. The partitioned approach enables the use of separate domain solvers whose solutions couple at the fluid-solid interface in the FSI-DCG time-stepping algorithm. For the fluid domain, we used an existing scheme for the Euler equations of gas dynamics based on a second-order extension of Godunov’s method with an approximate Roe Riemann solver. The solver for the equations of nonlinear elasticity is a second-order characteristic-based upwind method, which extends a previous numerical approach for linearly elastic solids. The new solid-domain solver incorporates small high-order dissipation terms to stabilize the contributions of the characteristic variables associated with zero eigenvalues of the first-order system of equations for the solid. The scheme also includes a stress-strain relaxation term to ensure that the stress-strain compatibility condition is nearly satisfied.

An important contribution of the present work is the analysis of a fluid-solid Riemann problem at the interface. The solution of the problem, obtained using the method of characteristics and the matching conditions at the interface, provides formulas for the normal velocity and stress on the interface in terms of impedance-weighted averages of the values for the fluid and solid on either side of the interface. The interface states given by these formulas are used in a projection step of the AMP algorithm. Two versions of this interface projection are derived, a full projection and a simplified projection, and it is found that numerical solutions obtained using either projection are nearly identical although the simplified projection is easier to implement and computationally less costly. The AMP algorithm with either projection is accurate and stable, even for the case of light solids when added-mass effects are large.

Four FSI problems were considered to verify the accuracy and stability of the AMP algorithm. An FSI model problem involving an elastic piston configuration was considered. Numerical solutions were computed using the AMP algorithm on a sequence of composite grids with increasing grid resolution and compared with an exact solution constructed using the method of analytic solutions. Maximum norm errors were computed to verify the order of accuracy of the numerical solutions. The second problem considered involved a rotating elastic disk immersed in a fluid. A semi-analytic exact solution was obtained assuming circular symmetry of the problem, and this solution was used to verify the accuracy and stability of solutions computed using the AMP algorithm (without assuming any symmetry) for the cases of heavy, medium and light solids. The errors in the solutions computed using a traditional partitioned (TP) algorithm were found to be similar to those obtained using the AMP algorithm for the heavy solid case. The TP algorithm was not stable for the medium and light solid cases. A third FSI problem involving a planar shock impacting a light elliptical-shaped solid was computed with the AMP algorithm using the neo-Hookean (NE) and linear elastic (LE) constitutive solid models. The results were also compared with solutions computed assuming a rigid elliptical solid. It was found that the NH and LE solutions agreed well at a time just after the initial shock impact when the solid deformation was small. The subsequent evolution of the NH solid, however, showed significant rotation so that the NH and LE solutions were not close at later times, as expected. The behavior of the

solid for the rigid case, on the other hand, was found to be reasonably close to that for the NH case. A comparison of solutions for the NH model using grids of different resolution indicated stability and grid convergence for this complex FSI problem. Finally the flow of a high speed gas past a light, thin and flexible solid beam was simulated in order to demonstrate the effectiveness of the AMP algorithm and deforming composite grids to treat problems with large deformations. Computations were performed for beams with different material properties, and very large deformations of the beam centerline were observed, especially for the lightest beam considered. Grid convergence studies were presented which showed excellent agreement for the position of the beam centerline.

Extensions of the present work to FSI problems in three dimensions using the FSI-DCG approach together with parallel adaptive mesh refinement is under present consideration. Further active research includes the development of AMP algorithms for FSI problems with other fluid and solid models.

## References

- [1] J. W. Banks, W. D. Henshaw, D. W. Schwendeman, Deforming composite grids for solving fluid structure problems, *J. Comput. Phys.* 231 (9) (2012) 3518–3547.
- [2] J. W. Banks, W. D. Henshaw, B. Sjögreen, A stable FSI algorithm for light rigid bodies in compressible flow, *J. Comput. Phys.* 245 (2013) 399–430.
- [3] J. W. Banks, B. Sjögreen, A normal mode stability analysis of numerical interface conditions for fluid/structure interaction, *Commun. Comput. Phys.* 10 (2) (2011) 279–304, .
- [4] J. W. Banks, W. D. Henshaw, D. W. Schwendeman, An analysis of a new stable partitioned algorithm for FSI problems. Part I: Incompressible flow and elastic solids, *J. Comput. Phys.* 269 (2014) 108–137.
- [5] J. W. Banks, W. D. Henshaw, D. W. Schwendeman, An analysis of a new stable partitioned algorithm for FSI problems. Part II: Incompressible flow and structural shells, *J. Comput. Phys.* 268 (2014) 399–416.
- [6] L. Li, W. D. Henshaw, J. W. Banks, D. W. Schwendeman, G. A. Main, A stable partitioned FSI algorithm for incompressible flow and deforming beams, arXiv preprint arXiv:1507.06041, submitted for publication (2015).
- [7] W. D. Henshaw, D. W. Schwendeman, An adaptive numerical scheme for high-speed reactive flow on overlapping grids, *J. Comput. Phys.* 191 (2003) 420–447.
- [8] W. D. Henshaw, D. W. Schwendeman, Moving overlapping grids with adaptive mesh refinement for high-speed reactive and non-reactive flow, *J. Comput. Phys.* 216 (2) (2006) 744–779.
- [9] D. Appelö, J. W. Banks, W. D. Henshaw, D. W. Schwendeman, Numerical methods for solid mechanics on overlapping grids: Linear elasticity, *J. Comput. Phys.* 231 (18) (2012) 6012–6050.
- [10] G. H. Miller, P. Colella, A conservative three-dimensional Eulerian method for coupled solid-fluid shock capturing, *J. Comput. Phys.* 183 (1) (2002) 26–82.
- [11] C. Farhat, J.-F. Gerbeau, A. Rallu, FIVER: A finite volume method based on exact two-phase Riemann problems and sparse grids for multi-material flows with large density jumps, *J. Comput. Phys.* 231 (19) (2012) 6360–6379.
- [12] V. Lakshminarayan, C. Farhat, A. Main, An embedded boundary framework for compressible turbulent flow and fluid-structure computations on structured and unstructured grids, *Int. J. Numer. Meth. Fl.* 76 (6) (2014) 366–395.
- [13] J. Donea, S. Giuliani, J. P. Halluex, An arbitrary Lagrangian-Eulerian finite element method for transient dynamic fluid-structure interactions, *Comput. Method. Appl. Mech. Engrg.* 33 (1982) 689–723.
- [14] R. Löhner, C. Yang, J. D. Baum, H. Luo, D. Pelessone, C. M. Charman, The numerical simulation of strongly unsteady flow with hundreds of moving bodies, *Int. J. Numer. Meth. Fl.* 31 (1999) 113–120.

- [15] E. Kuhl, S. Hulshoff, R. de Borst, An arbitrary Lagrangian Eulerian finite-element approach for fluid-structure interaction phenomena, *Int. J. Numer. Meth. Eng.* 57 (2003) 117–142.
- [16] H. T. Ahn, Y. Kallinderis, Strongly coupled flow/structure interactions with a geometrically conservative ALE scheme on general hybrid meshes, *J. Comput. Phys.* 219 (2006) 671–696.
- [17] I. Borazjani, L. Ge, F. Sotiropoulos, Curvilinear immersed boundary method for simulating fluid structure interaction with complex 3D rigid bodies, *J. Comput. Phys.* 227 (2008) 7587–7620.
- [18] J. T. Grétarsson, N. Kwatra, R. Fedkiw, Numerically stable fluid-structure interactions between compressible flow and solid structures, *J. Comput. Phys.* 230 (8) (2011) 3062–3084.
- [19] F. Cirak, R. Deiterding, S. P. Mauch, Large-scale fluid-structure interaction simulation of viscoplastic and fracturing thin-shells subjected to shocks and detonations, *Computers & Structures* 85 (11-14) (2007) 1049–1065, Fourth MIT Conference on Computational Fluid and Solid Mechanics.
- [20] M. Arienti, P. Hung, E. Morano, J. E. Shepherd, A level set approach to Eulerian-Lagrangian coupling, *J. Comput. Phys.* 185 (1) (2003) 213–251.
- [21] P. T. Barton, B. Obadia, D. Drikakis, A conservative level-set based method for compressible solid/fluid problems on fixed grids, *J. Comput. Phys.* 230 (2011) 7867–7890.
- [22] J. Glimm, J. W. Grove, X. L. Li, D. C. Tan, Robust computational algorithms for dynamic interface tracking in three dimensions, *SIAM J. Sci. Comput.* 21 (1999) 2240–2256.
- [23] J. Du, B. Fix, J. Glimm, X. Jia, X. Li, Y. Li, L. Wu, A simple package for front tracking, *J. Comput. Phys.* 213 (2006) 613–628.
- [24] R. van Loon, P. D. Anderson, F. N. van de Vosse, S. J. Sherwin, Comparison of various fluid-structure interaction methods for deformable bodies, *Comput. Struct.* 85 (11-14) (2007) 833–843, Fourth MIT Conference on Computational Fluid and Solid Mechanics.
- [25] T. E. Tezduyar, S. Sathe, R. Keedy, K. Stein, Space-time finite element techniques for computation of fluid-structure interactions, *Comput. Method. Appl. Mech. Engrg.* 195 (17-18) (2006) 2002–2027.
- [26] M. Schäfer, I. Teschauer, Numerical simulation of coupled fluid-solid problems, *Comput. Method. Appl. Mech. Engrg.* 190 (2001) 3645–3667.
- [27] L. C. Wilcox, G. Stadler, C. Burstedde, O. Ghattas, A high-order discontinuous Galerkin method for wave propagation through coupled elastic-acoustic media, *J. Comput. Phys.* 229 (24) (2010) 9373–9396.
- [28] W. D. Henshaw, A high-order accurate parallel solver for Maxwell’s equations on overlapping grids, *SIAM J. Sci. Comput.* 28 (5) (2006) 1730–1765.
- [29] F. C. Dougherty, J.-H. Kuan, Transonic store separation using a three-dimensional Chimera grid scheme, paper 89-0637, AIAA (1989).
- [30] R. Meakin, Moving body overset grid methods for complete aircraft tiltrotor simulations, paper 93-3350, AIAA (1993).
- [31] F. Zahle, J. Johansen, N. N. Sørensen, J. M. R. Graham, Wind turbine rotor-tower interaction using an incompressible overset grid method, paper 2007-425, AIAA (2007).
- [32] W. M. Chan, Overset grid technology development at NASA Ames Research Center, *Comput. Fl.* 38 (3) (2009) 496–503.
- [33] D. D. J. Chandar, M. Damodaran, Numerical study of the free flight characteristics of a flapping wing in low Reynolds numbers, *AIAA J. Aircraft* 47 (1) (2010) 141–150.

- [34] W. D. Henshaw, K. K. Chand, A composite grid solver for conjugate heat transfer in fluid-structure systems, *J. Comput. Phys.* 228 (2009) 3708–3741.
- [35] W. D. Henshaw, D. W. Schwendeman, Parallel computation of three-dimensional flows using overlapping grids with adaptive mesh refinement, *J. Comput. Phys.* 227 (16) (2008) 7469–7502.
- [36] G. S. Chesshire, W. D. Henshaw, Composite overlapping meshes for the solution of partial differential equations, *J. Comput. Phys.* 90 (1) (1990) 1–64.
- [37] W. D. Henshaw, The Overture hyperbolic grid generator, user guide, version 1.0, Research Report UCRL-MA-134240, Lawrence Livermore National Laboratory (1999).
- [38] W. D. Henshaw, Ogen: An overlapping grid generator for Overture, Research Report UCRL-MA-132237, Lawrence Livermore National Laboratory (1998).
- [39] D. W. Schwendeman, C. W. Wahle, A. K. Kapila, The Riemann problem and a high-resolution Godunov method for a model of compressible two-phase flow, *J. Comput. Phys.* 212 (2006) 490–526.
- [40] M. Ozlem, D. Schwendeman, A. Kapila, W. Henshaw, A numerical study of shock-induced cavity collapse, *Shock Waves* 22 (2012) 89–117.
- [41] B. Gustafsson, H.-O. Kreiss, J. Olinger, *Time Dependent Problems and Difference Methods*, John Wiley and Sons Inc., 1995.
- [42] P. J. Roache, Code verification by the method of manufactured solutions, *ASME J. of Fluids Engineering* 124 (1) (2002) 4–10.
- [43] G. B. Whitham, *Linear and Nonlinear Waves*, John Wiley and Sons, New York, 1974.
- [44] W. D. Henshaw, Mappings for Overture, a description of the Mapping class and documentation for many useful Mappings, Research Report UCRL-MA-132239, Lawrence Livermore National Laboratory (1998).